

Chapter 2

Stiffness Analysis for Grasping Tasks

Giuseppe Carbone

Abstract This section addresses key aspects that are related with stiffness properties when dealing with grasping tasks. Main theoretical aspects are formulated for computing the Cartesian stiffness matrix via a proper stiffness analysis and modeling. Basic concepts are given for the comparison of stiffness performance for different robotic architectures and end-effectors by referring both to local and global properties. Cases of study are described for clarifying the effectiveness and engineering feasibility of the proposed formulation for stiffness analysis. Then, an experimental set-up and tests are proposed for the experimental validation of stiffness performance.

2.1 Introduction

A load applied on a body produces deformations of the body itself that are known as compliant displacements. Stiffness can be defined as the property of a mechanical system in sustaining loads without too large compliant displacements. Stiffness can be also defined quantitatively as the amount of force that can be applied in one direction per unit of compliant displacement of the body in the same direction, or the ratio of a steady force acting on a body to the resulting compliant displacement [1–8].

Stiffness plays a key role both in the design and control of any robotic system for grasping tasks. Thus, stiffness is widely investigated for any robotic system

G. Carbone (✉)

LARM: Laboratory of Robotics and Mechatronics, University of Cassino and South Latium,
Via G. Di Biasio, 43 03043 Cassino, FR, Italy
e-mail: carbone@unicas.it

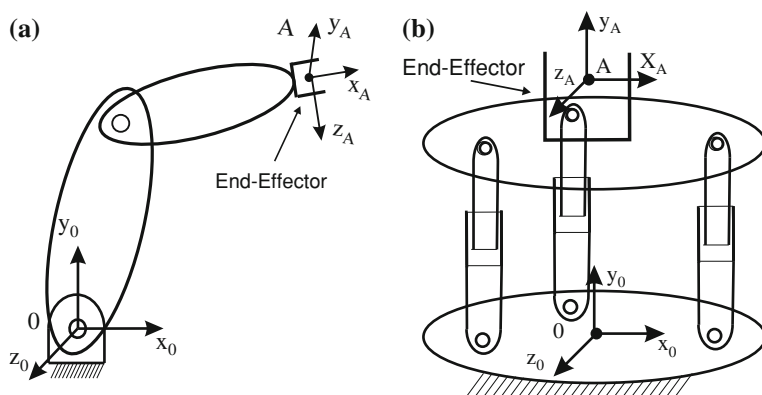


Fig. 2.1 Schemes of multibody robotic systems: **a** A 2R serial manipulator; **b** A parallel manipulator with three RPR legs

spanning from conventional serial robots to non-conventional parallel manipulators, such as those that are schematized in Fig. 2.1. Few examples in a wide literature can be found in [6–28].

Given the peculiarities of grasping tasks, one should carefully study the stiffness performance of the robotic system but also of the robot extremity, which is generally denominated as end-effector. In fact, usually only the end-effector is directly interacting with the environment and the objects that have to be manipulated. There are many different types of end-effectors with different sizes, shapes, operation, and actuations principles, as stated for example in [2, 29–31]. Stiffness can be considered of particular significance for all those mechanically achieving the grasp. They may range from dedicated mechanical grippers having two fingers (widely used in industrial applications) up to versatile multi-fingered robotic hands (widely investigated for mimicking the high multi-purpose operation of human hands). Some examples from an extensive literature are reported in [32–40].

Several grasping devices have been also designed and built at LARM in Cassino, [41–49]. For example, Fig. 2.2 shows two prototypes at LARM: a two-finger gripper, Fig. 2.2a, and a robotic hand with three fingers, Fig. 2.2b, respectively.

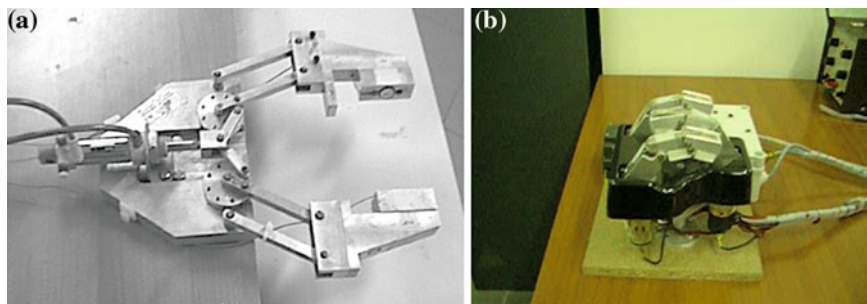


Fig. 2.2 Example of grasping devices that have been designed and built at LARM in Cassino: **a** A two-finger gripper; **b** The LARM Hand IV with three fingers

Many researchers have investigated stiffness with different approaches and focuses. Most of the published works on stiffness can be classified into three main categories. The first category deals with stiffness analysis and determination of overall stiffness. Given the stiffness of main components motors, joints, links, the overall stiffness has to be determined as reported, for example, in [7–18]. Once a proper stiffness model has been defined it can be used for controlling the grasp stability, or in compliance control algorithms as proposed for example in [19–21]. Moreover, a proper stiffness model can be used also for design purposes, for example, in order to find an optimum compromise between weight of links and stiffness performance as proposed in [22–24]. A second category studies the inverse decomposition of a stiffness matrix into constituent stiffness parameters that are often assumed to be simple linear springs, as proposed for example in [25]. In a third research line, mathematical properties of the stiffness matrix are investigated, mainly with the aim of finding intrinsic properties that are independent from the coordinate frame in which the stiffness matrix is expressed, [26–28].

Although stiffness is widely investigated there are still open problems. For example, experimental determinations and evaluations of stiffness performance are prescribed in standard codes for robotic manipulators, [50–52] that should be extended also to non-conventional robotic systems, grippers, and hands. Still an open issue can be considered also the formulation of computationally efficient algorithms that can give direct engineering insight of the design parameter influence and can be translated into experimental tests for experimental determinations. Moreover, still few preliminary comparisons of numerical results with experimental experience have been proposed, [53, 54].

2.2 Stiffness Modelling and Analysis

Usually, stiffness analysis of a robotic system is aiming to determine the stiffness performance through the computation of a 6×6 Cartesian stiffness matrix K . This stiffness matrix K expresses the relationship between the compliant displacements ΔS occurring to a frame fixed at the end of the kinematic chain when a static wrench W acts upon it and W itself. Considering Cartesian reference frames, 6×1 vectors can be defined for the compliant displacements ΔS and the external wrench W as

$$\begin{aligned}\Delta S &= (\Delta x, \Delta y, \Delta z, \Delta \alpha, \Delta \gamma, \Delta \delta)^t; \\ W &= (F_x, F_y, F_z, T_x, T_y, T_z)^t\end{aligned}\tag{2.1}$$

where Δx , Δy , Δz , $\Delta \alpha$, $\Delta \gamma$, and $\Delta \delta$ are the linear and angular compliant displacements on the robotic system extremity; F_x , F_y , and F_z are the force components acting on the robotic system extremity along X , Y , and Z directions, respectively; T_x , T_y , and T_z are the torque components acting upon the same point on the robotic system extremity about X , Y , and Z directions, respectively.

Compliant displacements have usually negative effects on a robotic device for grasping tasks, since compliance detrimentally affect accuracy, repeatability, and payload capability. Additionally, in dynamic conditions, the presence of large compliant displacements can affect fatigue strength, can produce vibrations and energy losses. However, in some cases, compliant displacements can even have a positive effect if they are properly controlled, [55,56]. In fact, they can enable the correction of misalignment errors encountered; for example, when parts are mated during assembly operations [5] or in peg into hole tasks [21], or in deburring tasks, [57], or in the operation of a prosthesis [58]. It is to note also that a stiffer behavior is often obtained at cost of an higher own weigh of a robotic system that can rise manufacturing costs and detrimentally affect dynamic performance and power consumption. Thus, a proper stiffness modeling and analysis is of key significance to identify optimal trade-off solutions both at design and control stage.

Provided that the assumptions of small compliant displacements hold, one can write

$$\mathbf{K}(q) : \mathbb{R}^r \rightarrow \mathbb{R}^r, \quad \mathbf{W} = \mathbf{K} \Delta \mathbf{S} \quad (2.2)$$

where \mathbf{K} is the so-called 6×6 Cartesian or spatial stiffness matrix.

It is worth noting that according to the definition in Eq. (2.2), the stiffness matrix \mathbf{K} is in general posture dependant. Moreover, the stiffness matrix \mathbf{K} is generally nonsymmetric and its entries depend on choice of reference frame, since it is not reference frame invariant, as demonstrated for example in [2, 7, 16, 26–28].

The computation of stiffness matrix \mathbf{K} can be achieved with different approaches such as finite element methods (FEM) or methods based on models with lumped parameters (MLP). FEM methods can be used for a stiffness analysis of multibody robotic systems, although with very difficult numerical implementation. In fact, even if FEM methods could be more accurate than MLP methods they are time consuming and they require a complete recalculation at each configuration/loading condition under analysis. Therefore, the stiffness analysis of robotic systems is usually carried out by means of MLP methods that are based on using lumped stiffness parameters for taking into account the stiffness properties of links and joints with configuration dependant relationships. Therefore, main advantages of MLP methods can be understood in reduced computational efforts and possibility to use the same stiffness model for the analysis of several different configurations. These aspects give the possibility to investigate the stiffness performance through the whole workspace of a robotic system in a reasonable amount of computational time. Moreover, MLP methods can be conveniently used for developing parametric models within optimal design procedures.

Equation (2.2) defines \mathbf{K} as a 6×6 matrix whose components are the amount of forces or torques that can be applied per unit of compliant displacements of the end effector for a robotic system. However, the linear expression in Eq. (2.2) is valid only for small magnitude of the compliant displacements $\Delta \mathbf{S}$. Moreover, Eq. (2.2) is valid only in static (or quasi static) conditions. The entries of a 6×6

stiffness matrix can be obtained through the composition of suitable matrices. A first matrix C_F gives all the wrenches \mathbf{W}_L , acting on the links when a wrench \mathbf{W} acts on the manipulator extremity as

$$\mathbf{W} = C_F \mathbf{W}_L \quad (2.3)$$

with the matrix C_F representing the force transmission capability of the manipulator mechanism.

A second matrix K_p gives the possibility to compute the vector $\Delta \mathbf{v}$ of all the deformations of the links when each wrench \mathbf{W}_{Li} on a i th link given by \mathbf{W}_L , acts on the legs according to

$$\mathbf{W}_L = K_p \Delta \mathbf{v} \quad (2.4)$$

with the matrix K_p grouping the lumped parameters of the robotic system.

A third matrix C_K gives the vector $\Delta \mathbf{S}$ of compliant displacements of the manipulator extremity due to the displacements of the manipulator links, as expressed as

$$\Delta \mathbf{v} = C_K \Delta \mathbf{S} \quad (2.5)$$

Therefore, the stiffness matrix K can be computed as

$$K = C_F K_p C_K \quad (2.6)$$

with matrix C_F giving the force transmission capability of the mechanism; K_p grouping the spring coefficients of the deformable components; C_K considering the variations of kinematic variables due to the deformations and compliant displacements of each compliant component.

Matrices C_K and C_F can be computed, for example, as a Jacobian matrix J and its transpose, respectively, as often proposed in the literature. Thus, one can compute the Cartesian stiffness matrix as

$$K = J^t K_p J \quad (2.7)$$

Nevertheless, this is only an approximate approach as pointed out, for example, in [59]. A more accurate computation of matrices C_K and C_F can be obtained as reported, for example in [2, 7, 13]. The K_p matrix can be computed as a diagonal matrix whose components are the lumped stiffness parameters of links, joints, and motors that compose a multibody robotic system. The lumped stiffness parameters can be estimated by means of analytical and empirical expressions or by means of experimental tests.

The lumped stiffness parameters can be graphically represented as linear or torsion springs. Examples of stiffness models with lumped parameters are shown in Fig. 2.3. In particular, Fig. 2.3a shows a stiffness model with lumped parameters for the 2R serial manipulator in Fig. 2.1a. This model considers the stiffness of the two motors and joints by means of two lumped parameters k_{T1} , k_{T2} .

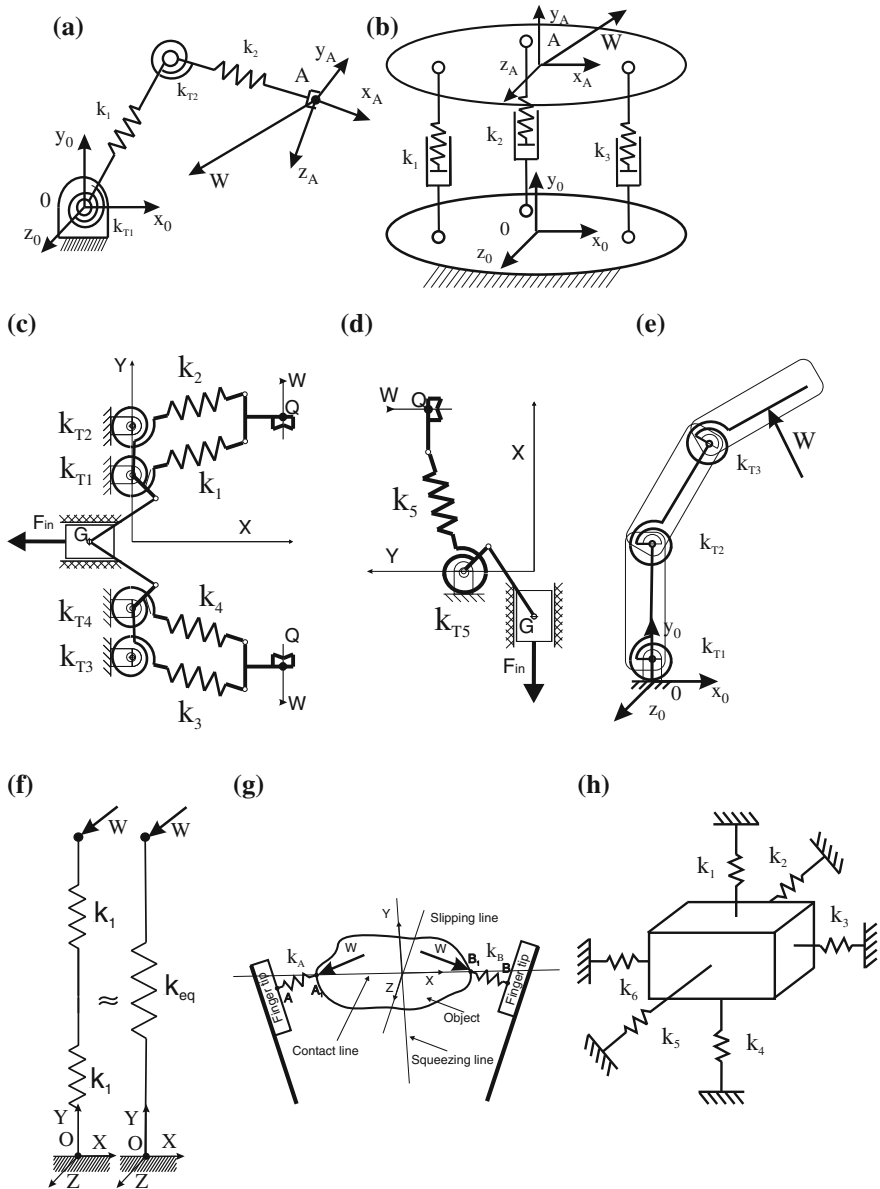


Fig. 2.3 Examples of stiffness models with lumped parameters: **a** For the 2R serial manipulator in Fig. 2.1a; **b** For the parallel manipulator in Fig. 2.1b; **c** For the two finger gripper in Fig. 2.2a; **d** For the symmetric part of the two finger gripper in Fig. 2.3c; **e** For one finger of the LARM Hand IV in Fig. 2.2b; **f** Two linear springs and their equivalent as a single linear spring; **g** For the grasping of a generic object with a two finger gripper; **h** For representing a generic stiffness matrix with a six linear springs model

Additionally, the axial stiffness of the links is considered by means of the lumped parameters k_1, k_2 . These two scalar lumped parameters can be replaced with two 6×6 stiffness matrices K_1, K_2 that can be even obtained by means of finite element softwares for taking into account the whole stiffness behavior of the links. Similarly, Fig. 2.3b shows a stiffness model with lumped parameters for the parallel manipulator in Fig. 2.1b. This model considers the stiffness of the two prismatic actuators and links by means of two lumped parameters k_1, k_2 . These two scalar lumped parameters can be replaced with two 6×6 stiffness matrices K_1, K_2 that can be even obtained by means of finite element softwares for taking into account the whole stiffness behavior of the links.

Figure (2.3c) shows a stiffness model for the two-finger gripper in Fig. 2.2a. This model takes into account the stiffness of joints and links by means of the lumped parameters $k_{T1}, k_{T2}, k_{T3}, k_{T4}$, and k_1, k_2, k_3, k_4 , respectively. It is to note that the two-finger gripper in Fig. 2.2a has a symmetric design. Thus, one can study only half of the model. Additionally, the effect of the lumped parameters k_{T1}, k_{T2} and k_1, k_2 , can be combined in the lumped parameters k_{T5} and k_5 , respectively, as shown in the simplified scheme of Fig. 2.3d. Similarly, Fig. 2.3e shows a simplified stiffness model for the robotic hand in Fig. 2.2b. In this simplified model, the stiffness properties of the motor and the driving mechanism as well as the flexional properties of the links have been combined in the lumped parameters k_{T1}, k_{T2}, k_{T3} . It is to note that it is advisable to keep the number of chosen lumped stiffness parameters as equal to the desired rank of the stiffness matrix (that is equal to six in the spatial case, to three in the planar case). In fact, choosing a different number of lumped stiffness parameters yields to nonsquare matrices that can lead to computation problems. For this purpose, if the superposition principle holds, one can combine the effect of more compliance sources in a single lumped parameter as described in the example of Fig. 2.3f where the lumped stiffness parameters k_1 and k_2 have been combined in the equivalent lumped parameter k_{eq} , whose value can be obtained as

$$(k_{eq})^{-1} = (k_1)^{-1} + (k_2)^{-1} \quad (2.8)$$

The grasping of an object also should require proper stiffness models that need to take into account the contact forces, the position of contact points/areas, the curvature of surfaces in contact. For example, Fig. 2.3f shows a simplified stiffness model with lumped parameters for the grasping of a generic object with a two-finger gripper. The contact areas on the two fingertips are assumed to coincide with the contact points A and B along the contact line. The stiffness properties of the contact are lumped in the parameters k_1, k_2 that are shown in Fig. 2.3f as ideal springs having no mass and length A-A₁ and B-B₁ equal to zero. The grasping model can become more complex as the one in Fig. 2.3f if one considers contact areas, multiple contact points, variable curvature of surfaces, and effect of friction on stiffness. In these cases, the scalar lumped parameters k_1, k_2 can be replaced by 6×6 stiffness matrices K_A and K_B . It is to note that any 6×6 stiffness matrix

can be decomposed in a model with linear springs having scalar lumped parameters such as the general model with six linear springs that is shown in Fig. 2.3g.

Stiffness properties usually have different expressions according to the chosen reference frame. Thus, each stiffness model should clearly indicate the chosen reference frame. For example, in two-finger grasping models as in Fig. 2.3f a Cartesian reference frame can be chosen with axes coinciding with the contact line, squeezing line, and slipping line.

The Cartesian stiffness matrix K is posture dependent. Thus, one should define configuration(s) of a multibody robotic system where the stiffness matrix can be computed. The configuration(s) should be carefully chosen in order to have significant information on the stiffness performance of the system in its whole workspace. Then, the kinematic model can be used for computing the vector θ that express input angles and strokes in the Joint Space for any posture. It is worth noting that the accuracy in the estimation of model data such as geometrical dimensions and values of lumped stiffness parameters can significantly affect the accuracy of the computed stiffness matrix. Thus, experimental tests should be carried out in order to validate model data and overall stiffness model.

Once the stiffness matrix has been computed, it is also necessary to give synthetic evaluation of the stiffness performance both for analysis and design purposes. Thus, an index of merit can be formulated by using properties of the stiffness matrix, so that it represents numerically the stiffness performance of a new multibody robotic system.

The current standard codes for stiffness evaluation of manipulators are given as short parts of the norms ANSI/RIA15.01.11-1990 [51] and ISO9283-1995 [52], which refer explicitly to serial chain industrial robots only. In particular, Sect. 8.6 in [51] and Sect. 10 in [52] are devoted to Static compliance with a very similar approach but only referring to a performance evaluation through measures of position compliant displacements. Then, a recommendation states to express the results in term of millimeters per Newton for displacements that are referred to the directions of a base coordinate system. Thus, the standard codes do not yet consider the stiffness matrix as a performance index for the elasto-static response of multibody robotic manipulators, but they still refer to a practical evaluation with a direct natural interpretation that is related to the compliance response of the stiffness of a manipulator structure. Of course, it is evident that compliant displacements can be considered as a measure of the manipulator stiffness since the fundamental relationship in Eq. (2.1). Nevertheless, the compliance response is system posture and wrench direction dependant since one can find a 6×1 vector of compliant displacements at any posture for any wrench. Therefore, one should define a single local index of stiffness performance and then a global index expressing the stiffness performance in the overall workspace of a multibody robotic system.

A local stiffness index can be directly related with the Cartesian stiffness matrix by means of different mathematical operators that can be applied to a matrix, as proposed for example in [54].

Compliant displacements can also provide an insight on local stiffness performance due to their simple physical interpretation, as indeed suggested by ISO and ANSI codes [51, 52]. In fact, one can compute the compliant displacements for a given configuration by multiplying the computed stiffness matrix for a given external wrench $\mathbf{W}_{\text{Given}}$. Reasonable choices for $\mathbf{W}_{\text{Given}}$ can be a unit vector or a vector equal to the expected payload for a multibody robotic system as proposed for example in [7]. The first choice gives a measure of the compliant displacements per unit of external wrench. The second choice provides a measure of the maximum compliant displacements for the system in specific applications. Nevertheless, compliant displacements have usually six components. Thus, they cannot be treated as a single merit index.

Eigenvalues and eigenvectors of a stiffness matrix are also very useful for their physical interpretation with respect to local stiffness performance. In fact, the eigenvectors are related with the maximum and minimum eigenvalue and they provide the directions of maximum and minimum stiffness performance, respectively. Moreover, a smaller difference among the eigenvalues stands for a smaller anisotropic stiffness behavior at a given posture. Nevertheless, eigenvalues and eigenvectors cannot be treated as a single merit index. But their values can be used for drawing graphical local representations of the stiffness performance such as compliance/stiffness ellipses and ellipsoids, as reported for example in [8]. These graphical local representations also provide a graphical tool for the comparison of stiffness performance along and about different directions. The graphical representations can be very useful when specific design requirements arise. In particular, they are useful if there is a need of the best stiffness performance only in a given direction or if equal stiffness is preferred in all directions.

Other graphical tools for a comparison of stiffness performance can be obtained through the definition of the so-called center of stiffness or the center of compliance and by means of stiffness or compliant axes that can be used for defining directions and orientations in which a robotic system acts as a simple spring, as mentioned for example in [22].

A local index of stiffness performance is neither suitable for an accurate design analysis nor useful for a comparison of different designs. In fact, even if a robotic system has suitable stiffness for a given system posture it can have inadequate stiffness at other postures. Therefore, one should look at stiffness performance at all points of workspace or define a single global stiffness index over the whole workspace yet.

A global index of stiffness performance for a robotic system can be defined with graphical methods that are based on plotting curves connecting postures having the same value of the local stiffness index (iso-stiffness curves or surfaces), as proposed for example in [6]. Nevertheless, the number of iso-stiffness curves or surfaces that one can plot is graphically limited. Moreover, few curves or surfaces usually do not provide sufficient insight of the overall stiffness behavior of a robotic system. These aspects significantly reduce the effectiveness of iso-stiffness curves or surfaces.

Global stiffness indices can be defined also in a mathematical form by using minimum, maximum, average, or statistic evaluations of a local stiffness index. For example, one can compute a global index in the form

$$GI_{MN} = \frac{\int \max_{i=1,\dots,6} \{ \sqrt{\lambda_i^*} \} dV}{L^3} \quad (2.9)$$

where $\{ \sqrt{\lambda_i^*} \}$ is the set of nonnegative eigenvalues of KK^T V is the workspace volume; L is a characteristic length that is used in order to obtain information that is independent from the workspace volume. Alternatively to L^3 , the denominator can be expressed as the volume V of workspace. Moreover, the dimensional inconsistency can be solved by using a proper dimensionless value of the merit index (that is indicated with a superscript $*$) that can be obtained by dividing the length entries by a characteristic length L . This global index can be useful when a design goal is to maximize the stiffness performance along or about one or more specific direction(s). A similar global stiffness index can be defined by referring to the minimum eigenvalue as

$$GI_{mN} = \frac{\int \min_{i=1,\dots,6} \{ \sqrt{\lambda_i^*} \} dV}{L^3} \quad (2.10)$$

This global stiffness index can be useful to detect and avoid design with weak stiffness performance along or about a specific direction. A global index can be defined also as the difference between GI_{MN} and GI_{mN} .

It is to note that the integration operator in Eqs. (2.9) and (2.10) is usually numerically calculated, since the analytical expression of $\{ \sqrt{\lambda_i^*} \} dV$ is usually not available. Thus, for comparison purposes it is advisable to have the same number of calculation configurations.

2.3 Numerical Computation of Stiffness Performance

The models and formulations in the previous section can be used to get a numerical insight of the stiffness performance for a robotic system. In particular, a numerical algorithm can be composed of a first part in which all the model data are provided such as the numerical values of the geometrical dimensions, masses, and lumped stiffness parameters. A second part defines the kinematic model, the force transmission model, and the lumped parameter model through the matrices C_F , C_K , and K_p , respectively. Then, a third part can compute an expression of the stiffness matrix K by means of Eqs. (2.6) or (2.7), as shown in the flowchart of Fig. 2.4.

It is worth noting that the matrices C_F , and C_K as well as the Jacobian matrix and its transpose are configuration dependant. Thus, they may have nonlinear components in a complex formulation. In general, this makes very difficult to

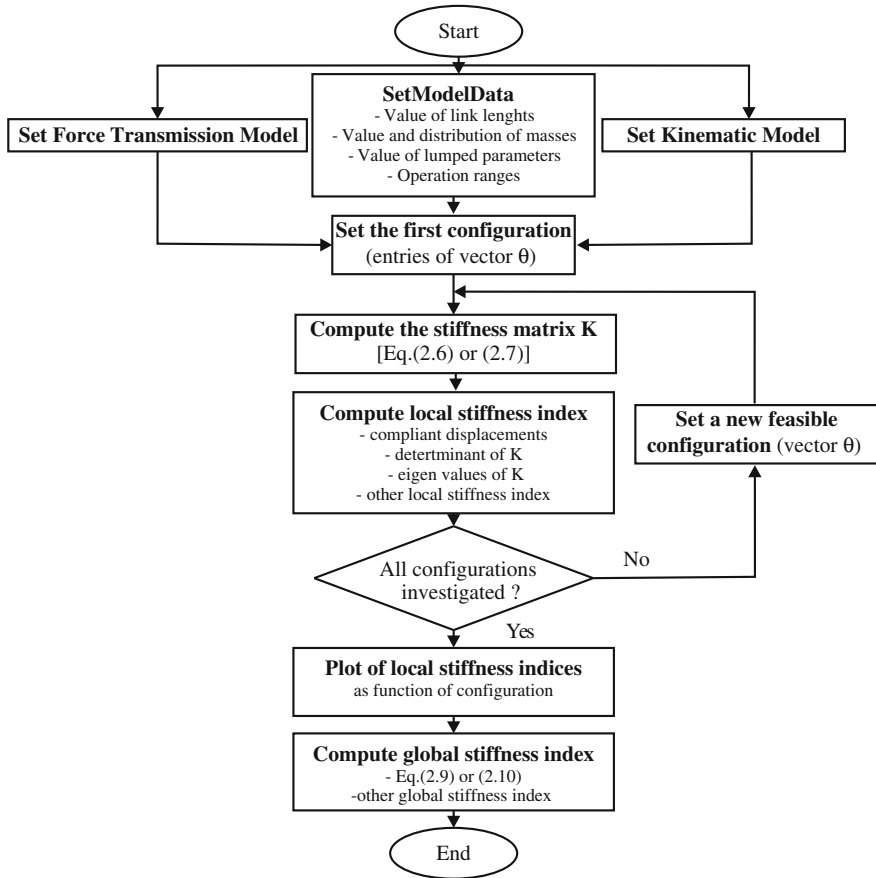


Fig. 2.4 A flowchart for the proposed numerical computation of stiffness performance

identify a close-form formulation of the stiffness matrix K . Thus, often the matrices C_F and C_K or the Jacobian matrix are numerically computed at a given configuration, and then combined into Eqs. (2.6) or (2.7) to calculate the stiffness matrix K . However, one should carefully define the configuration(s) where the stiffness matrix will be computed. The configuration(s) should be carefully chosen in order to have significant information on the stiffness performance of the system in its whole workspace. Careful attention should be addressed also to avoid numerical singularities for the stiffness matrix K that might occur also due to nonlinear terms. However, a linearization might be possible under the assumption of small compliant displacements.

Once the stiffness matrix has been computed, it can compute local stiffness indices at a given configuration. Different local stiffness indices can be chosen as also mentioned in the previous section. Values of local stiffness indices allow to compare the stiffness performance of a robotic system at different configurations.

An iterative loop can be defined to investigate a significant (but finite) number of configurations within the workspace of a robotic system. In some cases, a robotic system can have few trajectories that are mostly used during its operation. In these cases, the kinematic model can be used together with a proper path planning strategy for properly computing the time evolution of all the entries in the vector θ that express input angles and strokes in the joint space as function of time for a given trajectory. Thus, the vector $\theta(t)$ can be used for computing the stiffness matrix as function of time for a given end-effector trajectory.

After completing the calculation of the local stiffness indices one can plot their values as function of the configuration. Additionally, one can plot other graphical representations of stiffness properties such as the iso-stiffness curves. Finally, one can compute the global stiffness parameter, for example, by using Eqs. (2.9) or (2.10). These global values are useful for quantitative comparisons of different robotic systems especially at design stage.

It is to note that a proper stiffness analysis of a robotic system for grasping tasks should start from the identification of the main sources of compliance. In fact, there is always a trade-off between accuracy of the model and computational costs. For this reason, very often the stiffness analysis is limited to the robot architecture while one should carefully consider also the end effector.

2.4 Cases of Study for Stiffness Modelling and Analysis

2.4.1 A 6R Serial Manipulator

A 6 DOFs PUMA-like manipulator has been considered as a case of study for the above-mentioned formulation as specifically applied to a serial type robotic system. Main design parameters for a PUMA-like manipulator are shown in Fig. 2.5a.

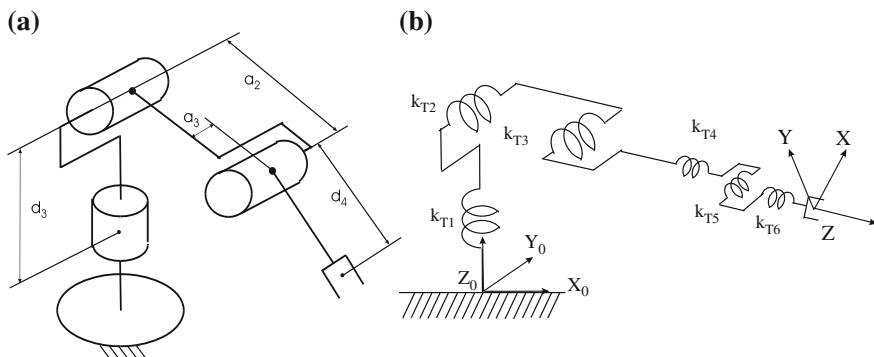


Fig. 2.5 Models for a PUMA-like manipulator: **a** Main dimensional parameters; **b** Lumped stiffness parameters

Table 2.1 Main design parameters and workspace ranges for a PUMA 562

a_2 (mm)	a_3 (mm)	d_3 (mm)	d_4 (mm)	x (mm)	y (mm)	z (mm)	ϕ (°)	ψ (°)	θ (°)
431.8	20.3	125.4	431.8	529.2	472.4	625.0	180	180	180

Values of the design parameters a_2 , a_3 , d_3 , and d_4 are reported in Table 2.1. These values have been defined by referring to a PUMA 562 design and the mobility ranges for the joint angles have been assumed equal to 180° for the first three joints (of the arm) and 90° for the last three joints (of the wrist).

A simplified stiffness model for a PUMA-like manipulator is shown in Fig. 2.5b. In this model, the links have been considered as rigid bodies. In fact, in this type of robots, the payloads are limited and the compliant displacements are in general due to the flexibility of joints only. The link compliant displacements are much smaller than the compliant displacements that are due to the compliance of motors as pointed out for example in [44]. Thus, in the model of Fig. 2.5b the lumped parameters k_{T1} to k_{T6} take into account the stiffness motors and joints only.

Moreover, if the only contributions to the overall compliance are given by motor compliances, the stiffness matrix K can be computed through Eq. (2.7) where J is the well-known Jacobian matrix of the PUMA-like robot. The matrix K_P in Eq. (2.7) can be computed as a diagonal matrix with lumped stiffness parameters of the motors that can be set as $k_{T1} = k_{T2} = k_{T3} = 5 \times 10^6$ Nm/rad and $k_{T3} = k_{T4} = k_{T5} = 5 \times 10^4$ Nm/rad as reasonable values by referring to a PUMA 562. The stiffness matrix of the PUMA-like robot that can be computed through Eq. (2.7) as function of the input joint angles. The expressions of the input joint angles can be computed as functions of the coordinates $(x, y, z, \phi, \psi, \theta)$ for the position and orientation of the end effector from the well-known inverse Kinematics of PUMA-like robot.

It is worth noting that the accuracy in the estimation of model data such as geometrical dimensions and values of lumped stiffness parameters can significantly affect the accuracy of the stiffness matrix that is computed through Eq. (2.7). Thus, experimental tests should be carried out in order to validate stiffness model and model data.

Results of the proposed stiffness analysis as applied to the PUMA-like architecture are reported in Table 2.2 and Figs. 2.6 and 2.7.

Table 2.2 Maximum values of compliant displacements and values of global stiffness indices within the feasible workspace of PUMA 562

Δx (mm)	Δy (mm)	Δz (mm)	$\Delta \phi$ (°)	$\Delta \psi$ (°)	$\Delta \theta$ (°)	GIMn	GImn
1.81	1.76	1.98	1.80	2.73	2.75	5.6202e + 034	5.3184e + 017

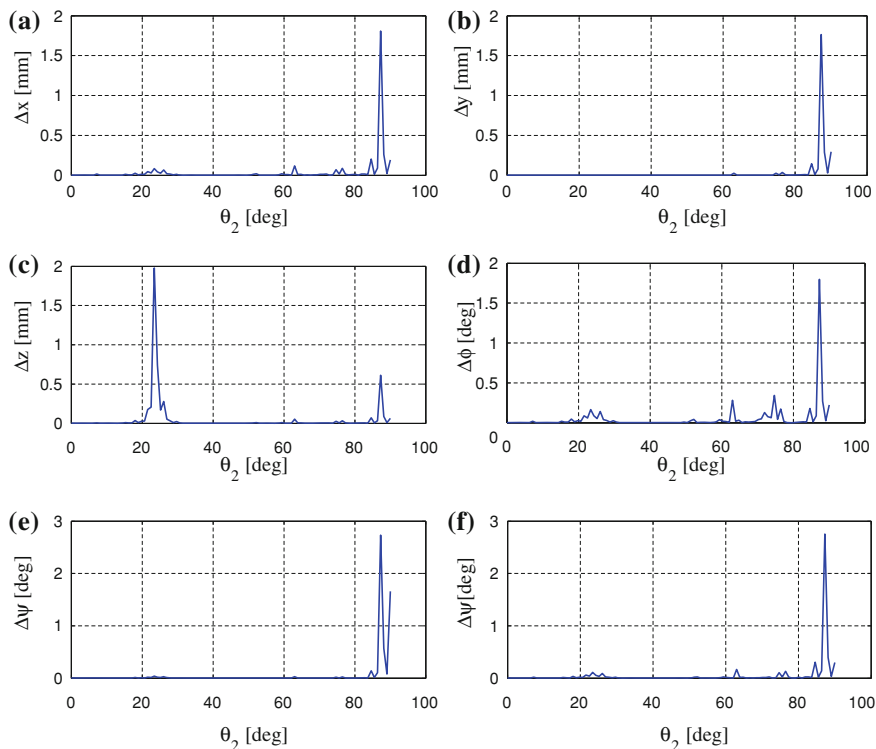


Fig. 2.6 Compliant displacements of Puma-562 as a function of the input angle θ_2 : **a** Linear compliant displacement along X-axis; **b** Linear compliant displacement along Y-axis; **c** Linear compliant displacement along Z-axis; **d** Angular compliant displacement about X-axis; **e** Angular compliant displacement about Y-axis; **f** Angular compliant displacement about Z-axis

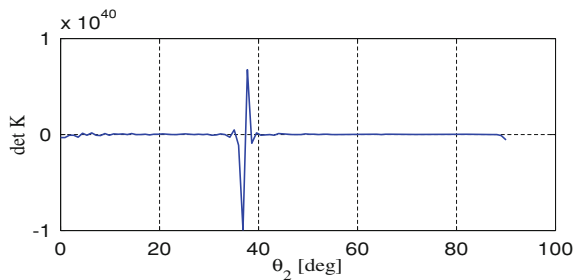


Fig. 2.7 Determinant of the matrix K for the case in Fig. 2.6

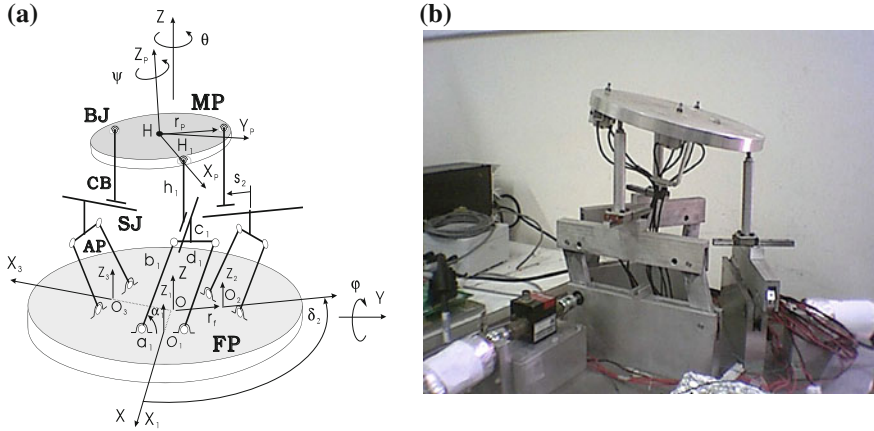


Fig. 2.8 CaPaMan (Cassino Parallel Manipulator) design: **a** A kinematic diagram; **b** A built prototype at LARM

2.4.2 A 3 DOF Parallel Manipulator

The Cassino parallel manipulator (CaPaMan) has been considered to test the engineering feasibility of the above-mentioned formulation as specifically applied to parallel architectures which can be different from a general Gough-Stewart platform. CaPaMan architecture has been conceived at LARM in Cassino since 1996, where a prototype has been built for experimental activity. A schematic representation of the CaPaMan manipulator is shown in Fig. 2.8a, and the prototype is shown in Fig. 2.8b. Indeed, by using the existing prototype, simulations have been carried out to compute its stiffness performance.

Kinematics of CaPaMan manipulator has been already investigated in previous works at LARM. In particular, matrices A and B have been formulated in the form

$$A = \begin{bmatrix} (D - F)b_1c\alpha_1 & (D + 2F)b_2c\alpha_2 & -(2D + F)b_3c\alpha_3 \\ (D + F)b_1c\alpha_1 & -Db_2c\alpha_2 & -Fb_3c\alpha_3 \\ b_1c\alpha_1 & b_2c\alpha_2 & b_3c\alpha_3 \end{bmatrix} \quad (2.11)$$

$$B = \begin{bmatrix} (6E/\sqrt{3}) & 0 & 0 \\ 0 & \sqrt{E(9r_p^2 - 4E)} & 0 \\ 0 & 0 & 3 \end{bmatrix} \quad (2.12)$$

in which

$$\begin{aligned} E &= z_1^2 + z_2^2 + z_3^2 - z_1z_2 - z_2z_3 - z_1z_3 \\ D &= 2z_2 - z_1 - z_3; \quad F = 2z_3 - z_1 - z_2 \end{aligned} \quad (2.13)$$

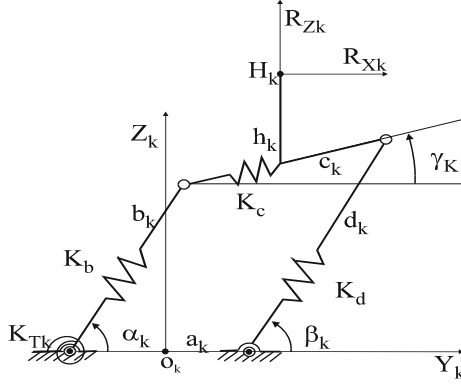


Fig. 2.9 A scheme for stiffness evaluation of a CaPaMan leg

with

$$z_k = b_k \sin \alpha_k; \quad \text{for } k = 1, 2, 3 \quad (2.14)$$

By modeling each leg of CaPaMan as in Fig. 2.9, the stiffness matrix of CaPaMan can be computed by using Eq. (2.6) with

$$C_F = M_{FN}; \quad C_K = C_P^{-1} A_d^{-1} \quad (2.15)$$

where M_{FN} is a 6×6 transmission matrix for the static wrench applied on H and transmitted to points H_1 , H_2 and H_3 of each leg; K_p is a 6×6 matrix with the lumped stiffness parameters of the three legs; C_p is a 6×6 matrix giving the displacements of the links of each leg as a function of the displacements of points H_1 , H_2 , and H_3 ; A_d is a 6×6 matrix that has been obtained by using the Direct Kinematics of the CaPaMan to give the position of point H on the movable plate as function of the position of points H_1 , H_2 , and H_3 in the form

$$\mathbf{X}_H = A_d \mathbf{v} \quad (2.16)$$

with $\mathbf{v} = [y_1, z_1, y_2, z_2, y_3, \Delta z_3]^T$ and $\mathbf{X}_H = [x_H, y_H, z_H, \varphi, \theta, \psi]^T$. The derivation of matrices M_{FN} , K_p , A_d , and C_p for CaPaMan can be found in [18].

The lumped stiffness parameters have been assumed as $k_{bk} = k_{dk} = 2.6 \times 10^6$ N/m and $k_{Tk} = 58.4 \times 10^3$ Nm/rad; the couplers c_k have been assumed rigid bodies because of the massive design that has been imposed to have a fix position of the sliding joints. Further, details on the derivation of the matrices in Eqs. (2.15) and (2.16) can be found in [18]. In the numerical example, for evaluation and design purposes we have assumed $r_p = r_f$, $a_k = c_k$, $b_k = d_k$.

Results of numerical simulations are shown in Figs. 2.10 and 2.11, while main numerical results for stiffness performance are summarized in Table 2.3.

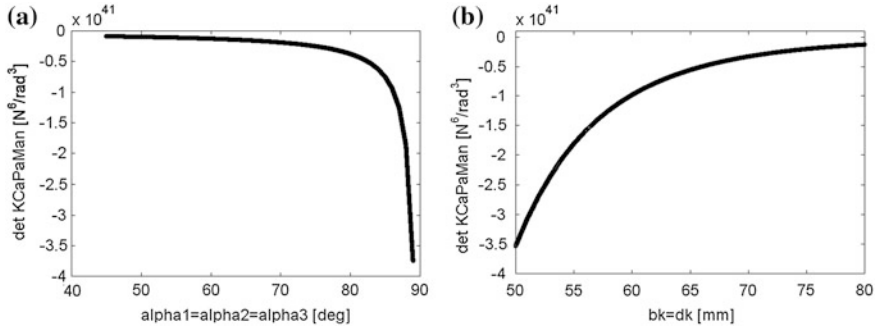


Fig. 2.10 Plots of the determinant of $K_{CaPaMan}$: **a** Versus $\alpha_1 = \alpha_2 = \alpha_3$; **b** Versus $b_k = d_k$ ($k = 1, 2, 3$) with $\alpha_1 = \alpha_2 = \alpha_3 = 60^\circ$

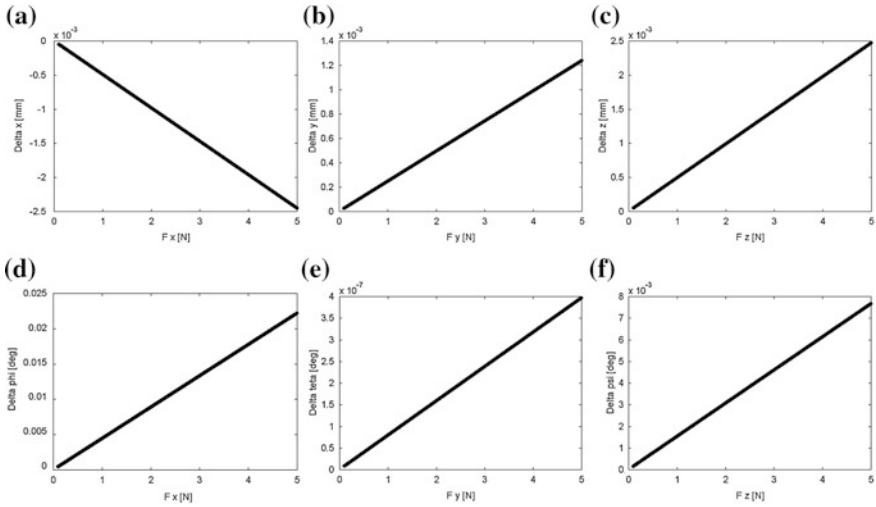


Fig. 2.11 Compliant displacements of CaPaMan as a function of $F_x = F_y = F_z$ when $N_x = N_y = N_z = 0$ for $\alpha_1 = \alpha_2 = \alpha_3 = 60^\circ$: **a** Δx ; **b** Δy ; **c** Δz ; **d** $\Delta \phi$; **e** $\Delta \theta$; **f** $\Delta \psi$

Table 2.3 Maximum values of compliant displacements and values of global stiffness indices within the feasible workspace of CaPaMan with $\mathbf{W} = (1.0; 1.0; 1.0; 0.0; 0.0; 0.0)^t$

Δx (mm)	Δy (mm)	Δz (mm)	$\Delta \phi$ (°)	$\Delta \psi$ (°)	$\Delta \theta$ (°)	GIMn	GImn
-0.0982	0.0309	0.0357	5.7932	0.0000	1.8620	4.8367e + 019	1.2882e + 017

Table 2.4 Illustrative value of forces as a function of the dimension L of an iron grasped object

Law	Type of force	Force [N] (at L = 1 mm)	Force [N] (at L = 100 mm))
$k_v L$	Van der Waals	0.119 $k_v = 1.19 \cdot 10^2$	$1.19 \cdot 10^{-9}$ $k_v = 1.19 \cdot 10^{-10}$
$k_e L^2$	Electro-static	0.014 $k_e = 1.40 \cdot 10^4$	$1.36 \cdot 10^{-6}$ $k_e = 1.36 \cdot 10^{-12}$
$k_G L^3$	Gravity	$3.00 \cdot 10^{-5}$ $k_G = 3.00 \cdot 10^4$	30.0 $k_G = 3.00 \cdot 10^4$
$k_I L^4$	Inertia	$3.06 \cdot 10^{-9}$ $k_I = 3.06 \cdot 10^3$	0.306 $k_I = 3.06 \cdot 10^3$
$k_m L^4$	Magnetic force	$1.00 \cdot 10^{-6}$ $k_m = 1.00 \cdot 10^5$	$1.00 \cdot 10^{-1}$ $k_m = 1.00 \cdot 10^5$
$k_g L$	Grasping force	1 $k_g = 1 \cdot 10^3$	300 $k_g = 3 \cdot 10^3$

2.4.3 A Two-Finger Milli-Gripper

The modeling and analysis of any grasping device should take into account its peculiarities and constraints. For example, the modeling and analysis of a milli-gripper should take into account many aspects including expected accuracy, dimensions, displacement ranges, acting forces, and loads. For example, the required accuracy can be considered inversely proportional to the geometric dimensions since smaller objects require greater positioning accuracy. The displacement and force capability are directly proportional to the geometric dimensions, since bigger objects require larger displacements of fingers and greater grasping force. For these reasons, in manipulative tasks at small scale the needed accuracy is high, while displacement and force capability are of small magnitude in agreement with the dimensions of the handled objects, [47].

A stiffness model for a two-finger milli-gripper is quite similar to the one shown in Fig. 2.3, even if important differences must be considered such as the scale of the acting forces and the kind of contact between the object and the fingers. As regards the scaling of the acting forces, Table 2.4 can be deduced by using dimensional analysis, similitude laws and experimental measurements as shown for example in [47]. Table 2.4 illustrates the main forces and their proportionality to the geometric dimension L of a grasped object by using coefficients k_v , k_e , k_G , k_I , k_m , and k_g that summarize have been computed from theoretical and experimental results in the literature. Moreover, Table 2.1 shows numerical examples, giving the intensity of different types of forces that have been evaluated in the case of L having a size of 1 and 100 mm. These examples show that, when the grasped object is of millimeter order, forces due to gravity and inertia can be neglected. The action of Van der Waals forces and electrostatic forces is still negligible as compared with the required grasping force at millimeter scale. A further scale reduction can make adhesive forces more significant than grasping forces, so that the releasing of the object becomes the most critical phase at micro- or even nano-scale [59].

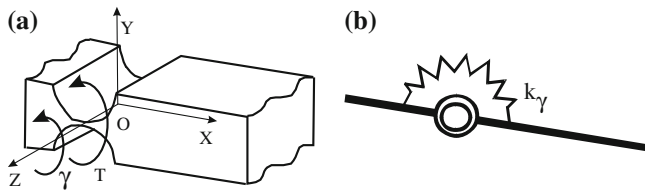


Fig. 2.12 A flexural joint: **a** Manufacturing scheme; **b** Kinematic model

The operation of a mechanical milli-gripper strongly depends on the design and behavior of the driving mechanism, which transmits the motion and force to the gripping fingers. Theoretically, a milli-gripper could have the same mechanism type of a conventional gripper. However, these mechanisms are not always feasible due to the small dimensions. In fact, for example, conventional joints cannot be easily miniaturized. This problem can be solved, for example, by using flexural joints. In fact, flexural joints can be manufactured from a single piece of material by using milling machines to provide a monolithic mechanism, which eliminates interface wear and allow very high miniaturization, as pointed out in [44, 46, 47].

Figure 2.12a and b shows a design scheme and a kinematic model for a flexural joint obtained by manufacturing two notches on a single piece of material to have rotations about the Z-axis related with the stiffness parameter k_γ . The stiffness about the X-axis and the Y-axis is much higher than about the Z-axis. Therefore, the rotations about the X-axis and the Y-axis can be neglected and the flexural joint allows only a rotation γ of few degrees about the Z-axis when a torque T is applied. Actual misalignment of the actuation force or any unexpected forces may cause rather large parasitic deflections in other direction than the desired one. However, generally, this is enough for the microworld applications.

Figure 2.13 shows a design solution that has been proposed at LARM in Cassino. It uses flexural joints to obtain four-bar Chebichev type driving mechanism that allows an approximately straight-line motion of the fingers as shown in the kinematic chain of Fig. (2.1c). Considering this specific planar case, one can

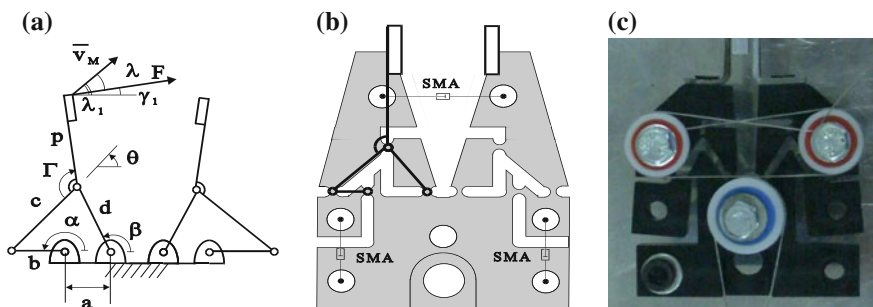


Fig. 2.13 A milli-gripper design: **a** Kinematic chain with design parameters; **b** A design scheme considering shape memory alloy (SMA) actuators; **c** A built prototype at LARM

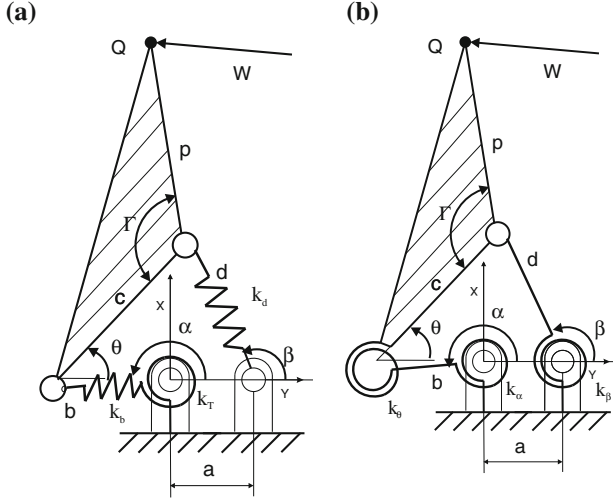


Fig. 2.14 Stiffness models with lumped parameters of the milli-gripper shown in Fig. 2.13: **a** With two linear and one torsional lumped parameters; **b** With three torsional lumped parameters

define the stiffness matrix K as a 3×3 . The vector of compliant displacements can be defined as $\Delta S = [\Delta x, \Delta y, \Delta \theta]^T$. The external acting wrench acting on the point Q can be defined as $W = [F_x, F_y, 0]^T$ when the external moment is assumed to be equal to zero. Referring to Fig. 2.13a a denotes the length of the frame, b and d are respectively the input and the output length links, and c is the length of the coupler whose fingertip point Q is located by the length p and the angle Γ .

Stiffness models of the milli-gripper in Fig. 2.13 can be proposed as shown in Fig. 2.14 by considering three lumped parameters. In particular, Fig. 2.14a shows a stiffness model with two linear lumped parameters that express the linear stiffness of the input and output links and one angular lumped parameter that express the stiffness of the input actuator and input flexural joint. Figure 2.14b shows a stiffness model with three angular lumped parameters that express the angular stiffness of the corresponding three flexural joints.

The bending of links and the stiffness of the actuator(s) can be also taken into account as additive components of these angular lumped parameters.

If OXY is a fixed reference and assuming that α is the input angle, positive counterclockwise, β the output angle, and θ the angle between the generic position of c and X-axis, from the loop closure equations one can write

$$\begin{aligned} x &= b \cos \alpha + c \cos \theta - p \cos(\Gamma - \theta) \\ y &= b \sin \alpha + c \sin \theta + p \sin(\Gamma - \theta) \\ \theta &= 2 \tan^{-1} \frac{\sin}{\alpha} - (\sin^2 \alpha + B^2 - D^2)^{1/2} B + D \end{aligned} \quad (2.17)$$

with x and y being the position of the point Q along the X - and Y -axis, respectively and with

$$\begin{aligned} B &= \cos \alpha - \frac{a}{b}; \quad C = \frac{a^2 + b^2 - c^2 + d^2}{2bd} - \frac{a}{d} \cos \alpha; \\ D &= \frac{a}{c} \cos \alpha - \frac{a^2 + b^2 + c^2 - d^2}{2bc} \end{aligned} \quad (2.18)$$

Thus, the kinematic equations (2.17) and (2.18) can be used to obtain the matrix C_k .

If one refers to the stiffness model in Fig. 2.13a, the static equilibrium can be expressed by referring to the equilibrium of the coupler as

$$\begin{vmatrix} F_x \\ F_y \\ T_z \end{vmatrix} = \begin{vmatrix} k_b \cos \alpha & k_d \cos \beta & -\frac{k_T}{b} \sin \alpha \\ k_b \sin \alpha & k_d \sin \beta & \frac{k_T}{b} \cos \alpha \\ k_b r_b & -k_d r_d & \frac{k_T}{b} r_T \end{vmatrix} \begin{vmatrix} \Delta b \\ \Delta d \\ \Delta \alpha \end{vmatrix} \quad (2.19)$$

with

$$\begin{aligned} r_b &= \frac{c}{2} \sin(\alpha + \theta) + p \cos(\alpha + \theta); \quad r_d = -\frac{c}{2} \sin(\alpha + \beta) + p \cos(\alpha + \beta); \\ r_T &= \frac{c}{2} \cos(\alpha - \theta) + p \sin(\alpha - \theta) \end{aligned} \quad (2.20)$$

where the moment of the forces has been computed about point Q .

By using Eq. (2.19) one can compute the product of the matrices C_F and K_P in the form

$$C_F K_P = \begin{vmatrix} k_b \cos \alpha & k_d \cos \beta & -\frac{k_T}{b} \sin \alpha \\ k_b \sin \alpha & k_d \sin \beta & \frac{k_T}{b} \cos \alpha \\ k_b r_b & -k_d r_d & \frac{k_T}{b} r_T \end{vmatrix} \quad (2.21)$$

Thus, Eqs. (2.17–2.21) can be used to compute the stiffness matrix K of the milli-gripper as described in Eq. (2.6).

It is to note that it is usually not simple to find a close form expression for the stiffness matrix even for a rather simple mechanism. A simplified expression of the stiffness matrix one can obtained by referring to the stiffness model in Fig. 2.6b and by using the Jacobian matrix of the proposed mechanism. For example, if one assumes $\Gamma = \pi$, $a = 0.005$, $b = 0.01$, $c = 0.005$, $d = 0.01$, $p = 0.01$ m, the Jacobian matrix can be computed as

$$J = \begin{bmatrix} \frac{-0.01 \sin \alpha + 0.02 \sin(\pi + a \sin(-2 \sin \beta + 2 \sin \alpha))}{\sqrt{1 - 4(\sin \beta - \sin \alpha)^2}} & -\frac{0.02 \sin(\pi + a \sin(-2 \sin \beta + 2 \sin \alpha)) \cos \beta}{\sqrt{1 - 4(\sin \beta - \sin \alpha)^2}} & -0.005 \sin \theta \\ 0.01 \sin \alpha & -\frac{0.02 \cos(\pi + a \sin(-2 \sin \beta + 2 \sin \alpha)) \cos \beta}{\sqrt{1 - 4(\sin \beta - \sin \alpha)^2}} & 0.005 \cos \theta \\ \frac{2 \sin(\alpha - \beta)}{\sin(\beta - \theta)} & 0 & 1 \end{bmatrix} \quad (2.22)$$

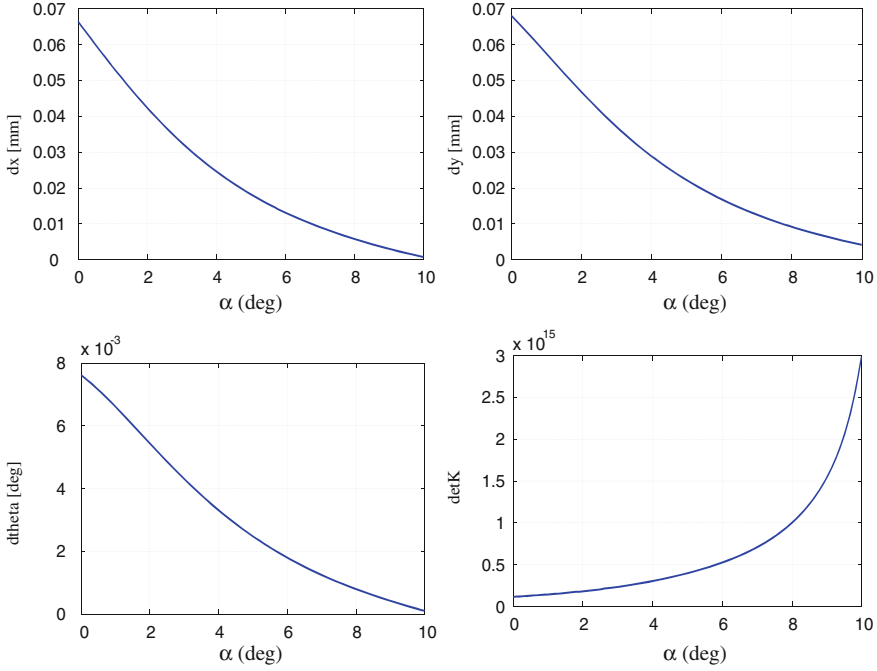


Fig. 2.15 Simulation results by referring to the model in Eqs. (2.15, 2.16) versus the value of the input angle α when $\mathbf{W}_{\text{Given}} = [1,1,0]^T$: **a** Linear compliant displacement along X-axis; **b** Linear compliant displacement along Y-axis; **c** Angular compliant displacement about Z-axis; **d** Determinant of the stiffness matrix \mathbf{K}

The matrix \mathbf{K}_p can be defined according to the model in Fig. 2.14b as

$$\mathbf{K}_p = \begin{vmatrix} k_\alpha & 0 & 0 \\ 0 & k_\beta & 0 \\ 0 & 0 & k_\theta \end{vmatrix} \quad (2.23)$$

Then, the Cartesian stiffness matrix can be easily obtained as in Eq. (2.7).

The stiffness matrix and compliant displacements can be computed at each configuration of the milli-gripper by means of Eqs. (2.17–2.21) or (2.22 and 2.23) by defining the values of the input angle and the values of the lumped stiffness parameters. For example, if one refers to the model in Fig. 2.14b, and one sets $k_\alpha = k_\beta = k_\theta = 10^6$ Nm/rad as reasonable values for the proposed milli-gripper, one can use Eqs. (2.22) and (2.23) to compute the stiffness matrix \mathbf{K} at any configuration. For example, the specific configuration when the input angle α is equal to zero yields

$$\mathbf{K} = 10^5 \begin{vmatrix} 4.1758 & -0.1215 & -1.9500 \\ -0.1215 & 0.4565 & -0.0979 \\ -1.9500 & -0.0979 & 1.0250 \end{vmatrix} \quad (2.24)$$

Table 2.5 Maximum values of compliant displacements and values of global stiffness indices within the feasible workspace of the milli-gripper in Fig. 2.13

Δx (mm)	Δy (mm)	Δz (mm)	GIMn	GImn
0.068	0.069	7.551 e-003	2.6422e + 008	3.2462e + 007

One can compute the stiffness matrix K at any other configuration by setting different values of the input angle α . A proper “for” loop can be implemented in any programming environment (such as Matlab) to span the whole operation range of the milli-gripper. The same code can be used to compute any local and global stiffness performance index as well as the compliant displacements at a given configuration for a given acting external wrench $\mathbf{W}_{\text{Given}}$.

For example, if one assumes $\mathbf{W}_{\text{Given}} = [1, 1, 0]^T$ then the complaint displacements versus the input angle α can be computed as shown in Fig. 2.15. The compliant displacements in Fig. 2.15 can be seen as local indices of stiffness performance. Similarly, the determinant of the stiffness performance can give an useful graphical information of the local stiffness performance as it grows when stiffness performance is improving. Global stiffness indices can be computed such as proposed in Eqs. (2.9) and (2.10) for the above-mentioned case of study as reported in Table 2.5.

2.4.4 LARM Hand IV

LARM Hand IV, Fig. 2.2b, is a robotic hand having three one-DOF human-like fingers that has been developed and built at LARM in Cassino. Figure 2.16 shows a scheme of a finger including a kinematic model of its driving mechanism. Each finger is basically composed of two four-bar linkage mechanisms as shown in Fig. 2.16. The first phalanx is the input bar of the first four-bar linkage mechanism. It is also the base frame of the second four-bar linkage mechanism. The second phalanx is the input bar of the second four-bar linkage mechanism and it is also the coupler of the first four-bar linkage mechanism. Then, the third phalanx is the coupler of the second four-linkage mechanism. Table 2.6 shows the main design parameters of a finger.

Referring to the scheme in Fig. 2.16, the angular velocities of the second and third phalanxes can be defined as $\dot{\theta}_g = d\theta_g/dt$ and $\dot{\theta}_j = d\theta_j/dt$, respectively. Both $\dot{\theta}_g$ and $\dot{\theta}_j$ can be computed as function of the input angular velocity of the first phalanx $\dot{\theta}_b = d\theta_b/dt$ in the form

$$\dot{\theta}_j = \dot{\theta}_g = \frac{b \sin(\theta_b - \theta_e)}{f \sin(\theta_e - \theta_f)} \dot{\theta}_b \quad (2.25)$$

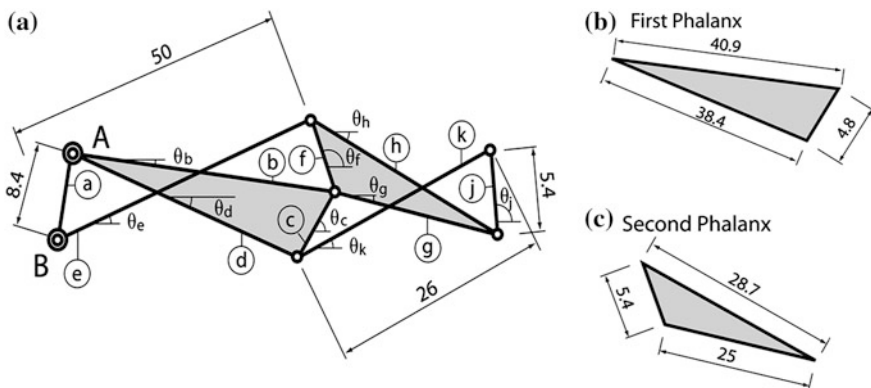


Fig. 2.16 Scheme of the LARM hand driving mechanism: **a** Complete system; **b** First phalanx; **c** Second phalanx

Table 2.6 Main design parameters of a finger of LARM Hand IV

	Frame	Phalanx 1				Phalanx 2				Phalanx 3	
		Phalanx body		Rod		Phalanx body		Rod		Phalanx body	
Label in Fig. 2.2	a	b	c	d	e	f	g	h	k	j	
Length (mm)	8.4	40.9	4.8	38.4	50	5.4	25	28.7	26	5.4	

$$\dot{\theta}_j = \dot{\theta}_c + \frac{g \sin(\theta_g - \theta_k)}{j \sin(\theta_k - \theta_j)} (\dot{\theta}_f - \dot{\theta}_c) \quad (2.26)$$

where one can also replace the angular velocity $\dot{\theta}_c$ with $\dot{\theta}_b$, since both $\dot{\theta}_c$ and $\dot{\theta}_b$ are angular velocities of the same rigid body (the first phalanx) with respect to the fixed reference frame. The time derivatives of Eqs. (2.25) and (2.26) can be also used for computing the angular accelerations on each phalanx. The above-mentioned kinematic equations can be used to derive the speed of each phalanx as function of the input speed or vice versa. Therefore, one can use Eqs. (2.25) and (2.26) for verifying that the speed of a phalanx provides a human-like behavior.

The LARM Hand IV is also equipped with three force sensors on each finger for measuring the grasping force on each phalanx. The location of these force sensors is shown in the scheme of Fig. 2.17a. It is worth noting that in the model of Fig. 2.3 each sensor has been modeled as a prismatic joint with a spring. The lumped stiffness parameter of each spring as been assumed as $k = 10 \text{ N/mm}$ by referring to a piezoresistive low-cost force sensor. Thus, the grasping force that is measured on each phalanx can be computed $F = k\Delta d$ where Δd is the compliant displacement on each spring.

Figure 2.17b shows a scheme of LARM hand grasping a cylindrical object. In this scheme, the object is in contact with the second phalanx of LARM Hand at point P. The same grasping conditions of Fig. 2.17 have been modeled in

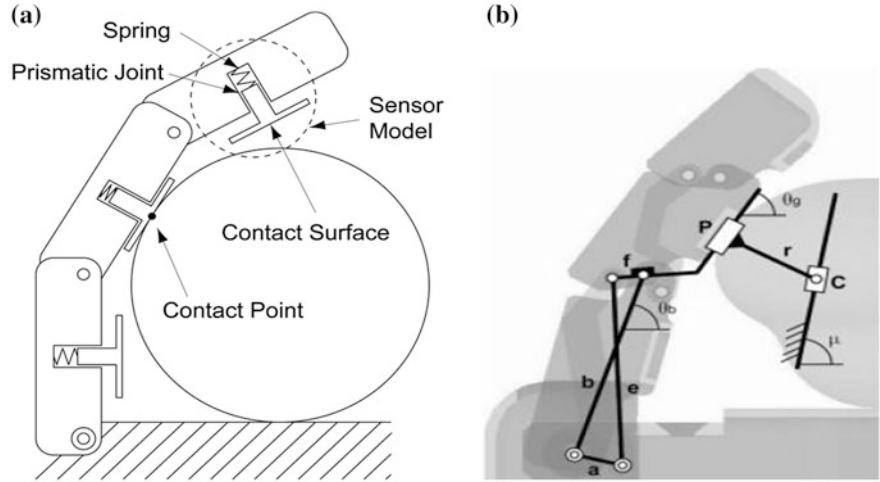


Fig. 2.17 A finger of LARM Hand IV: **a** Model of the grasp and contact; **b** A scheme of the kinematic chain for the numerical solution in MSC.ADAMS environment

MSC.ADAMS environment as shown in the scheme of Fig. 2.18. The proposed model in Fig. 2.18 has been carefully designed and implemented in order to obtain a suitable numerical solution of the proposed grasping conditions. It is worth noting that a firm grasp is achieved when all forces are in equilibrium. Therefore, the input torque has to change as function of several parameters including the external force acting on the object, and position, size, shape of the grasped object. Numerical simulations of LARM Hand operation have been computed in MSC.ADAMS environment.

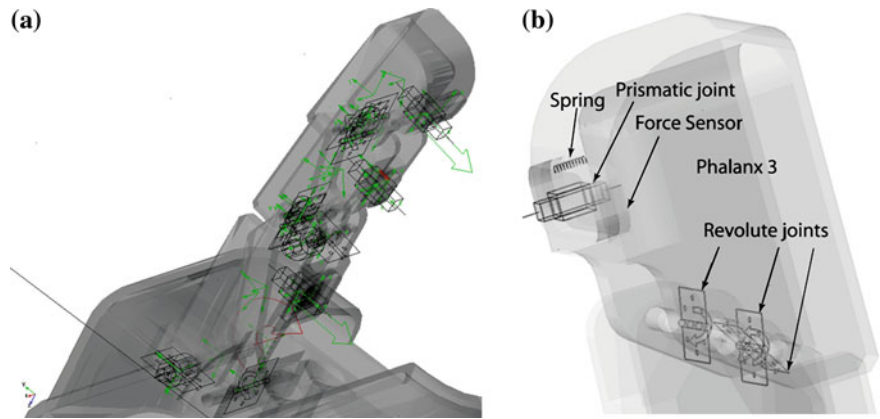


Fig. 2.18 A MSC.ADAMS mode of LARM Hand IV: **a** A finger with main constraints; **b** Detail of the third phalanx

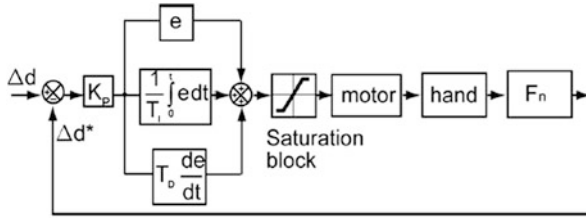


Fig. 2.19 Control PID with saturation block for the contact force control of the finger

The contact of the elastic bar with the frame and rollers have been modeled with the characteristic of the contact data as: stiffness: $1.0E11$ Pa; damping: $10.0E3$ Ns/m; force exponent: 2.2 N; maximum penetration: 0.1 mm. The friction has been modeled as a Coulomb force with the followings parameters: Static coefficient 0.6; Dynamic coefficient 0.5; Stiction Transition Velocity 100 mm/s; Friction Transition Velocity 1000 mm/s.

The operation mode is based on a control of the torque of the motor aiming to obtain a desired maximum value for the contact force. A close loop control is achieved by using as feedback the data that are obtained from force sensors on the finger. The force sensors are modeled as a linear spring as it is shown in Figs. 2.17a and 2.18b. The value of the contact force is obtained by evaluating the displacement of the prismatic joint of the force sensor. Figure 2.19 shows the scheme of the PID control with the input data that are obtained from the force sensor.

A saturation block has been added, as it is shown in Fig. 2.19. This block imposes upper and lower bounds on a signal. When the input signal is within the range specified by the lower limit and upper limit parameters, the input signal passes through unchanged. When the input signal is outside these bounds, the signal is set to the upper or lower bound. The system uses the measures that are provided by the force sensors to trigger the change from one control scheme to another. This trigger has been modeled with an “if” statements.

If the absolute value of the deformation of the spring that models a force sensor is lower than a threshold value the system remains in the speed control, but if the deformation is greater than this value the control switches to the contact force control. A hysteresic gap has been added to avoid an oscillation from one control to another in the transient phase between the two operation modes.

Several simulations have been carried out in MSC.ADAMS environment by implementing the proposed grasp model and control algorithm. Figures 2.20 and 2.21 show results of the simulation of LARM Hand IV while grasping a rigid cylinder of 50 mm of diameter, under various grasping conditions. The control has been designed to obtain a normal contact force of 1.5 N for the two parallel fingers and of 3 N for the opposite finger. A friction coefficient has been assumed at the contacts with low values, as in usual robotic devices.

The integrator is an algorithm that solves the differential equations of a dynamic problem over an interval of time during a simulation. The used integrator for the

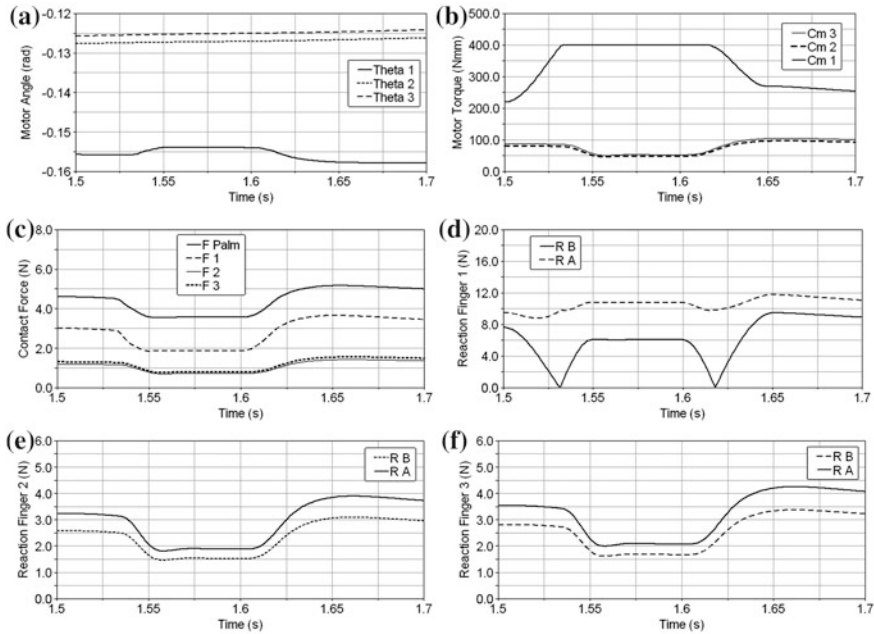


Fig. 2.20 Simulation results of the LARM Hand grasp in Fig. 2.3 when an external disturbing force is applied to the object: **a** Input angle; **b** Motor torque; **c** Contact grasp forces; **d** Reaction forces on finger 1; **e** Reaction forces on finger 2; **f** Reaction forces on finger 3

simulation has been gear stiff integrator (GSTIFF), [60]. The GSTIFF integrator is the default in MSC.ADAMS environment since it provides good solutions for simulation of stiff models. The GSTIFF integrator uses a backwards differentiation formula to integrate differential and algebraic equations. In addition, it assumes a fixed time step that results in fixed coefficients for predicting the errors. The time interval 0.1 (10 intervals in 1 s) has been selected after several attempts for developing the simulation of the LARM Hand in order to obtain suitable numerical results with suitable computational efforts. The simulation time has been 20 s in a standard Pentium II computer.

The speed control is used from the initial position until the spring suffer a compliant displacement of $\Delta d = 0.1$ mm. After this event occurs, the system switches to the contact force control. Results also show the transition from speed control to the contact force control. The PID constant $K_p = 1E4$, $K_i = 1E5$ and $K_d = 100$ has been chosen in order to prevent upper-oscillation around the value of the maximum force value.

Results in Figs. 2.20 and 2.21 show that the control is suitable for keeping a firm grasp. In particular, Fig. 2.20a shows the values for the angles of the input bars of the finger. These angles show that the finger does not return to its original configuration with input angle at -0.155 rad. However, the new input angle value of 0.153 rad is still a stable configuration. Figure 2.20b shows the motor torques that grow to their

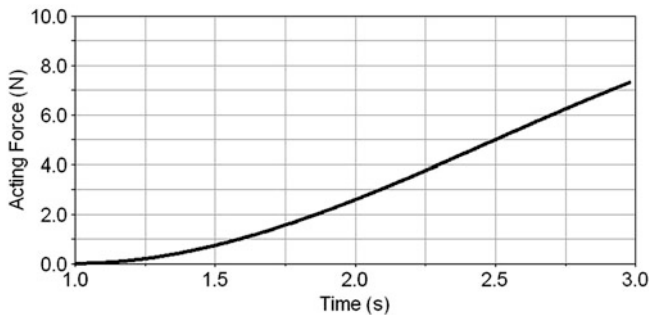


Fig. 2.21 Module of the external force that is applied to the centre of mass of the object that is grasped for the simulation, whose results are reported in Fig. 2.13

maximum value of 400 Nm in order to return to a new stable condition after about 0.15 s. The contact forces are shown in Fig. 2.20c. The control cannot avoid that the contact forces goes below the desired values of 3 N due to a restriction in the maximum torque that the input motor can provide. However, contact forces never go over 1.8 N. This value can be considered suitable for keeping the grasp and avoiding any damage to the objects to be grasped. Figures 2.20d–f show the reaction forces in the frame joints of the finger. In particular, plots in Fig. 2.20d show reaction forces ranging from 0 to about 12 N with sufficiently smooth time history, and Fig. 2.20e and d show reaction forces in the range from 1.5 to 4 N.

2.5 Experimental Determination of Stiffness Performance

Experimental determination of stiffness performance of multibody robotic systems can be performed for calibration purposes and operation characterizations by identifying the entries of stiffness matrix of the proposed formulation according to practical aims that can be related also to standard codes that are reported in [51, 52]. Nevertheless, the computation of the coefficients of the stiffness matrix requires carrying out experimental tests in which compliant displacements and wrenches will be measured contemporaneously.

One should note that the stiffness matrix K can be symmetric if and only if some conditions are satisfied on the external wrench and choice of reference frames for the representation of compliant displacements as demonstrated for example in [26–28]. Therefore, the computation of the 6×6 Cartesian stiffness matrix K in the most general case requires the identification of its overall 36 k_{ij} entries. The identification of all these 36 entries can be achieved if wrenches and compliant displacements are measured in at least six experiments for a given manipulator in a given configuration. In fact, with six experiments Eq. (2.2) can be used to give as many equations as the 36 unknown entries of K in the form

$$\begin{pmatrix}
{}^1\Delta x & {}^1\Delta y & {}^1\Delta z & {}^1\Delta \varphi & {}^1\Delta \psi & {}^1\Delta \theta & \dots & 0 & 0 & 0 & 0 & 0 & 0 \\
0 & 0 & 0 & 0 & 0 & 0 & \dots & 0 & 0 & 0 & 0 & 0 & 0 \\
0 & 0 & 0 & 0 & 0 & 0 & \dots & 0 & 0 & 0 & 0 & 0 & 0 \\
0 & 0 & 0 & 0 & 0 & 0 & \dots & 0 & 0 & 0 & 0 & 0 & 0 \\
0 & 0 & 0 & 0 & 0 & 0 & \dots & 0 & 0 & 0 & 0 & 0 & 0 \\
0 & 0 & 0 & 0 & 0 & 0 & \dots & {}^1\Delta x & {}^1\Delta y & {}^1\Delta z & {}^1\Delta \varphi & {}^1\Delta \psi & {}^1\Delta \theta \\
\vdots & \vdots & \vdots & \vdots & \vdots & \vdots & \dots & \vdots & \vdots & \vdots & \vdots & \vdots & \vdots \\
\vdots & \vdots & \vdots & \vdots & \vdots & \vdots & \dots & \vdots & \vdots & \vdots & \vdots & \vdots & \vdots \\
{}^6\Delta x & {}^6\Delta y & {}^6\Delta z & {}^6\Delta \varphi & {}^6\Delta \psi & {}^6\Delta \theta & \dots & 0 & 0 & 0 & 0 & 0 & 0 \\
0 & 0 & 0 & 0 & 0 & 0 & \dots & 0 & 0 & 0 & 0 & 0 & 0 \\
0 & 0 & 0 & 0 & 0 & 0 & \dots & 0 & 0 & 0 & 0 & 0 & 0 \\
0 & 0 & 0 & 0 & 0 & 0 & \dots & 0 & 0 & 0 & 0 & 0 & 0 \\
0 & 0 & 0 & 0 & 0 & 0 & \dots & 0 & 0 & 0 & 0 & 0 & 0 \\
0 & 0 & 0 & 0 & 0 & 0 & \dots & {}^6\Delta x & {}^6\Delta y & {}^6\Delta z & {}^6\Delta \varphi & {}^6\Delta \psi & {}^6\Delta \theta
\end{pmatrix}
\begin{pmatrix}
k_{11} \\ k_{12} \\ k_{13} \\ k_{14} \\ k_{15} \\ k_{16} \\ \vdots \\ \vdots \\ \vdots \\ k_{61} \\ k_{62} \\ k_{63} \\ k_{64} \\ k_{65} \\ k_{66}
\end{pmatrix}
-
\begin{pmatrix}
{}^1F_x \\ {}^1F_y \\ {}^1F_z \\ {}^1N_x \\ {}^1N_y \\ {}^1N_z \\ \vdots \\ \vdots \\ \vdots \\ {}^6F_x \\ {}^6F_y \\ {}^6F_z \\ {}^6N_x \\ {}^6N_y \\ {}^6N_z
\end{pmatrix}
=
\begin{pmatrix}
0 \\ 0 \\ 0 \\ 0 \\ 0 \\ 0 \\ \vdots \\ \vdots \\ \vdots \\ 0 \\ 0 \\ 0 \\ 0 \\ 0 \\ 0
\end{pmatrix}
\quad (2.27)$$

where the k_{ij} coefficients refer to the stiffness matrix as

$$K = \begin{bmatrix}
k_{11} & k_{12} & k_{13} & k_{14} & k_{15} & k_{16} \\
k_{21} & k_{22} & k_{23} & k_{24} & k_{25} & k_{26} \\
k_{31} & k_{32} & k_{33} & k_{34} & k_{35} & k_{36} \\
k_{41} & k_{42} & k_{43} & k_{44} & k_{45} & k_{46} \\
k_{51} & k_{52} & k_{53} & k_{54} & k_{55} & k_{56} \\
k_{61} & k_{62} & k_{63} & k_{64} & k_{65} & k_{66}
\end{bmatrix} \quad (2.28)$$

The numerical solution of Eq. (2.28) provides the required values of the 36 coefficients of the stiffness matrix in Eq. (2.14) once the wrenches (due to known masses) and compliant displacements (due to those wrenches) that have been measured in six experiments are available for a given configuration. These experiments can be carried out by means of Milli-CaTraSys that has been conceived and built at LARM as schematized in Fig. 2.22.

Milli-CaTraSys is a wire tracking system whose scheme is reported in Fig. 2.23. It is composed of six LVDT sensors that can measure the distances u_i ($i = 1, \dots, 6$). Then, the distances u_i are used as radii of arcs from corresponding center points O_i . The position of H on the robot end effector is defined as the position of the point at which three arcs intersect. Similarly, it is possible to measure the position of points F and Q. Then, the vectors connecting H, F, and Q can be used to determine the end-effector orientation through the orientation angles α , γ and δ , as shown in Fig. 2.22b. Thus, a trilateration technique can be used with Milli-CaTraSys in order to measure both position and orientation of its end effector that can be attached to a mobile body through reference points H, F and Q on it, as shown in Fig. 2.23. Moreover, that known masses can be attached on the free end of each wire as shown in Fig. 2.22a. Therefore, Milli-CaTraSys can measure the changes in position and orientation of its end effector (compliant displacements) while different known wrenches are applied. Several experimental trials can be carried out for each configuration just by applying different masses to the wires.

A virtual instrument in LabVIEW environment has been developed for acquisition and processing the data from the LVDT sensors. This virtual instrument has

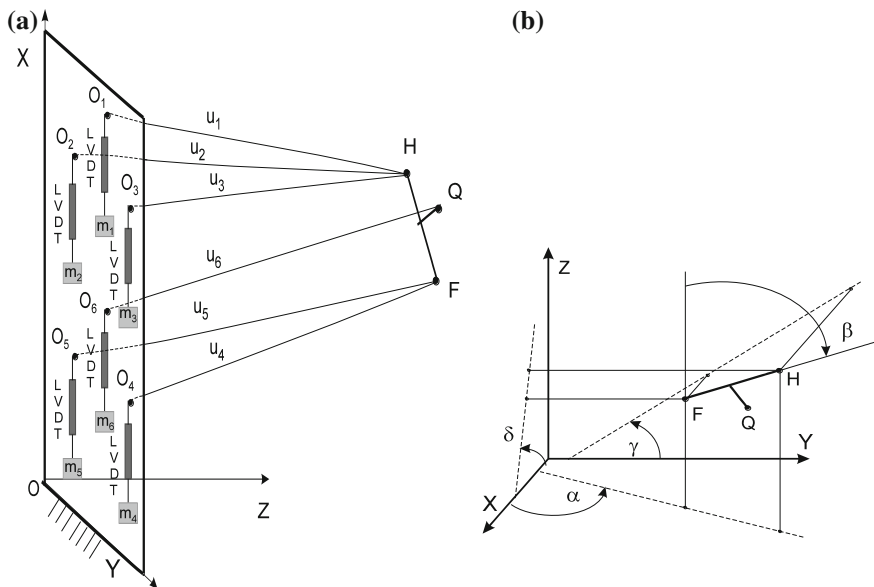


Fig. 2.22 A scheme of Milli-CaTraSys: **a** With the reference frame, LVDTs and masses m_i as applied to the wires u_i ($i = 1, \dots, 6$); **b** Orientation of the end-effector through the angles α , γ and δ

been used to measure the displacement of the cores inside the LVDT sensors. In this configuration of Milli-CaTraSys, the H point can be measured with any combination of three wires among the six available wires. In particular, the combination of three wires 1, 3, 5, and the combination of three wires 2, 4, 6 have been selected. In fact, these configurations are symmetric, have been proved to reduce computational costs, and increase the accuracy of measurement, as reported in previous experiences at LARM.

2.6 Cases of Study for Stiffness Experimental Tests

2.6.1 CaPaMan 2bis

CaPaMan 2bis is a parallel manipulator that has been designed and built at LARM in Cassino. A kinematic scheme of CaPaMan 2bis is shown in Fig. 2.23, where the fixed platform is FP and the moving platform is MP. MP is connected to FP through three identical leg mechanisms and is driven by the corresponding articulation points. An articulated parallelogram AP, a revolute joint RJ and a connecting bar CB compose each leg mechanism. AP's coupler carries the RJ and CB transmits the motion from AP to MP through RJ; CB is connected to the MP by a spherical joint BJ, which is installed on MP. Each plane, which contains AP, is

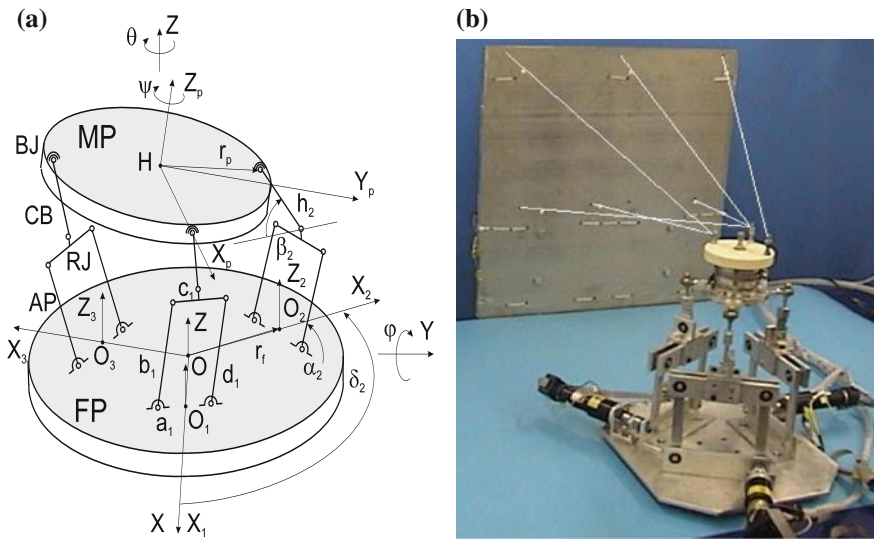


Fig. 2.23 The CaPaMan 2bis: **a** A kinematic scheme; **b** A prototype with Milli-CaTraSys set up at LARM in Cassino

rotated of $\pi/3$ with respect to the neighbour one. Design parameters of a k -th leg are identified through: a_k , which is the length of the frame link; b_k , which is the length of the input crank; c_k , which is the length of the coupler link; d_k , which is the length of the follower crank; h_k , which is the length of the connecting bar. The kinematic input variables are the crank angles α_k ($k = 1, 2, 3$). Sizes of MP and FP are given by r_p and r_f , respectively. Table 2.7 reports the sizes of main design parameters of CaPaMan 2bis.

Experimental tests have been carried out by applying six different wrenches for a given configuration of CaPaMan 2bis. In particular, Fig. 2.24 shows the measured compliant displacements when $m_1 = m_2 = m_3 = m_4 = m_5 = m_6 = 0.03$ kg and CaPaMan 2bis is in its vertical configuration. Similar results have been obtained for six different masses distributions. It is worth noting that the plots of Fig. 2.24 show the measured compliant displacements versus time during an static experiment. This is necessary in order to find the stationary values of the measured compliant displacements after applying the external wrench. In particular, the stationary values for the experimental test that is reported in Fig. 2.24 are $\Delta x = -0.041$, $\Delta y = 0.035$, $\Delta z = -0.155$, $\Delta \alpha = -1.964^\circ$, $\Delta \gamma = -1.667^\circ$ and $\Delta \delta = -0.277^\circ$.

Table 2.7 Sizes of main design parameters for CaPaMan 2bis

$a_k = c_k$ (mm)	$b_k = d_k$ (mm)	h_k (mm)	$r_p = r_f$ (mm)	α_k ($^\circ$)
100	100	50	65	45:135

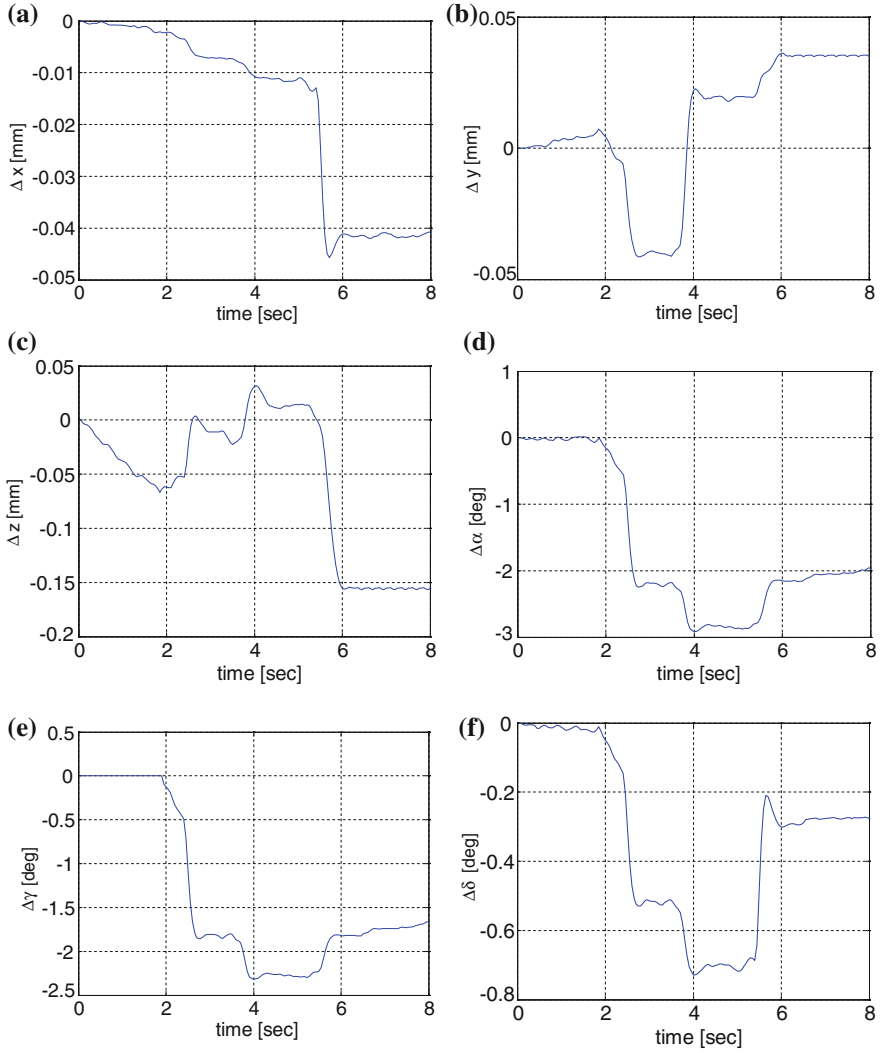


Fig. 2.24 Measured compliant displacements for a wrench given by $m_1 = m_2 = m_3 = m_4 = m_5 = m_6 = 0.033$ kg when CaPaMan2bis is in its vertical configuration: **a** Δx ; **b** Δy ; **c** Δz ; **d** $\Delta \alpha$; **e** $\Delta \gamma$; **f** $\Delta \delta$

The experimental analysis has given results, which confirm the numerical computations of the stiffness matrix. For example, when the three legs of CaPaMan 2bis are inclined of 45° the stiffness matrix is measured as given by

$$K = 10^8 \begin{bmatrix} 0.013 & 0.002 & 0.040 & -10.13 & 0.031 & 3.058 \\ 0.003 & 0.001 & 0.010 & -2.595 & 0.012 & 0.782 \\ 0.000 & 0.000 & 0.001 & -0.093 & -0.013 & 0.028 \\ 0.000 & 0.000 & 0.000 & -0.027 & 0.000 & 0.008 \\ -0.000 & -0.000 & -0.001 & 0.195 & -0.001 & -0.059 \\ 0.000 & 0.000 & 0.000 & -0.051 & 0.000 & 0.015 \end{bmatrix} \quad (2.29)$$

when wrenches are obtained by using additional masses of 50 grams on each wire once in tension.

When two legs are inclined of 60° and one leg is in vertical configuration, the stiffness matrix is measured as

$$K = 10^5 \begin{bmatrix} 0.014 & -0.094 & 0.268 & 7.416 & 4.410 & -2.051 \\ 0.009 & -0.174 & 0.606 & 1.740 & 13.99 & -5.299 \\ 0.008 & -0.138 & 0.500 & 20.09 & 7.603 & -5.923 \\ -0.000 & 0.000 & -0.000 & 0.003 & 0.007 & -0.000 \\ -0.000 & 0.000 & -0.001 & 0.169 & -0.026 & -0.050 \\ -0.000 & 0.000 & -0.000 & -0.307 & -0.126 & 0.092 \end{bmatrix} \quad (2.30)$$

The determinant of the stiffness matrix in Eq. (2.29) is equal to 5.987×10^{20} while the determinant of the stiffness matrix in Eq. (2.30) is equal to -2.452×10^{20} . By using this measure one can conclude that CaPaMan 2bis is stiffer in the first configuration, as intuitively expected.

2.6.1.1 LARM Hand IV

The attached problem is to determine the performance of the LARM Hand in terms of operation properties. This has been obtained by using the system Milli-CaTraSys. A proper end effector has been installed on a finger of the LARM Hand as shown in Fig. 2.25 and Fig. 2.26 in order to provide a proper location of points F, Q, and H and suitable frame for attaching the wires. In particular, three wires have been attached to point H, two wires to point F, and one wire to point Q. This setup refers to the Gough-Stewart 3-2-1 parallel manipulator configuration. Experiments with two redundant wires have been also carried out to have a 3-3-3 configuration and to validate the use of the 3-2-1 configuration with redundant measurement data.

A calibration process has been carried out on the experimental setup, as proposed for example in [24–27], in order to determine a suitable initial configuration for the measuring system and to verify its accuracy.

As a result of the experimental calibration process, it has been determined an average accuracy of Milli-CaTraSys of about 0.1 mm when LVDT sensors are used with 100 mm range and an accuracy of Milli-CaTraSys of about 0.01 mm when LVDT sensors are used with 2.5 mm range.

Experimental tests have been carried out by means of the setup that is shown in Fig. 2.25. In the experimental tests, pretension of all wires has been obtained by

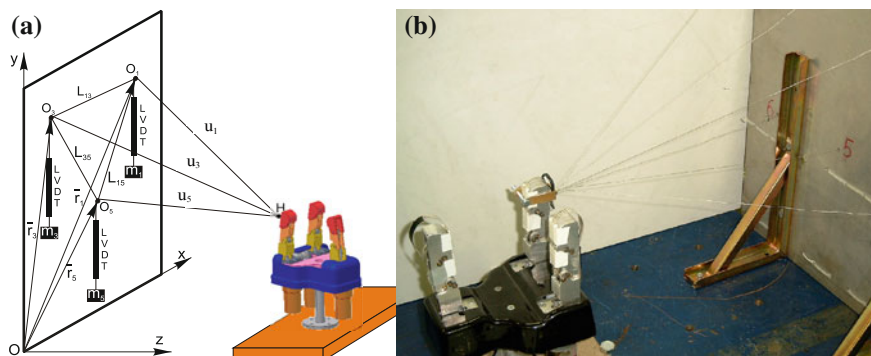


Fig. 2.25 The experimental set-up for the test-bed operations with LARM Hand: **a** A scheme; **b** The laboratory set-up

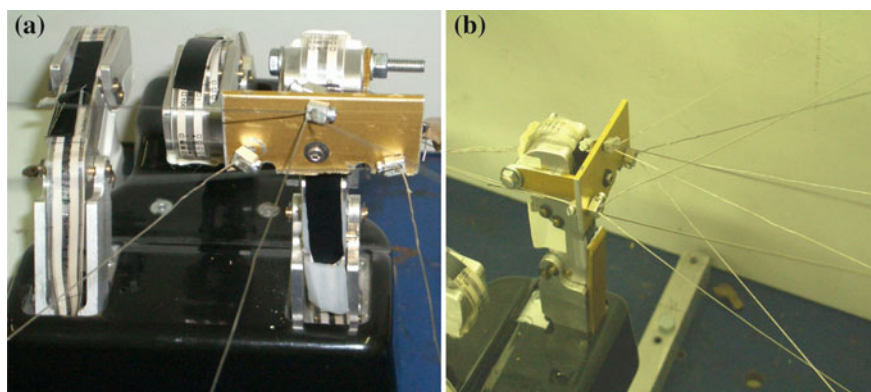


Fig. 2.26 End-effector for Milli-CaTraSys that has been attached to the fingertip of LARM Hand; **a** A zoomed frontal view with connections for six wires in a 3-2-1 platform configuration; **b** A zoomed lateral view with connections for six wires in a 3-3-3 platform configuration

means of known masses m_i ($i = 1, \dots, 6$) of 30 g. This pretension value has been set up experimentally since it keeps all the wires pulling during the whole duration of experimental tests. Moreover, this pretension produces negligible compliant displacements of the twisted iron wires that have been used in Milli-CaTraSys.

Experimental tests have been carried out by operating the LARM Hand in an open-close mode. Namely, the fingers of LARM Hand begin the tests in the fully open configuration; they start moving after about 1.6 s; they move to the fully closed configuration in about 1 s; they wait in the fully closed configuration about 2 s; they move back to the fully open configuration in about 1 s.

For example, Fig. 2.27 shows the plots of the measured lengths of the wires 1-3-5 during an experimental test. Then, the measured lengths of wires are converted through trilateration technique to give the position of the fingertip of LARM Hand.

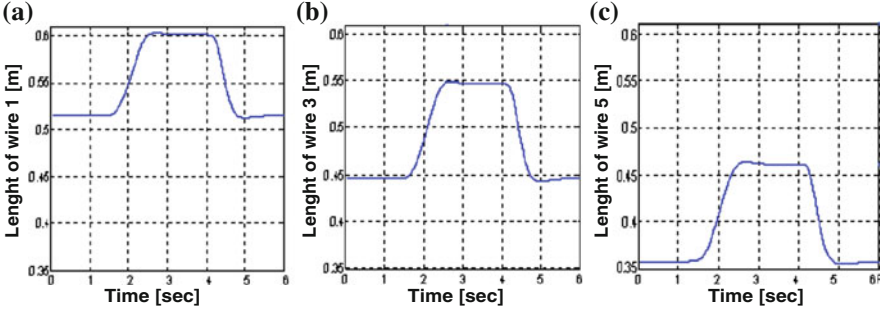


Fig. 2.27 Plots of the measured lengths of the wires of Milli-CaTraSys during an open-close operation mode for LARM Hand: **a** Wire 1; **b** Wire 3; **c** Wire 5

The position coordinates of the fingertip of LARM Hand during the experimental test in Fig. 2.27 are reported in Fig. 2.28 as function of time. In particular, Fig. 2.28a shows a 3D view of the operation workspace of a fingertip motion of LARM Hand in Cartesian coordinates. Figure 2.28b–d show the projection of the operation workspace of a fingertip motion of LARM Hand onto XY, YZ, and XZ planes, respectively. The measured motion ranges have been about 0.005 in X direction, 0.032 in Y direction, 0.113 m in Z direction, respectively.

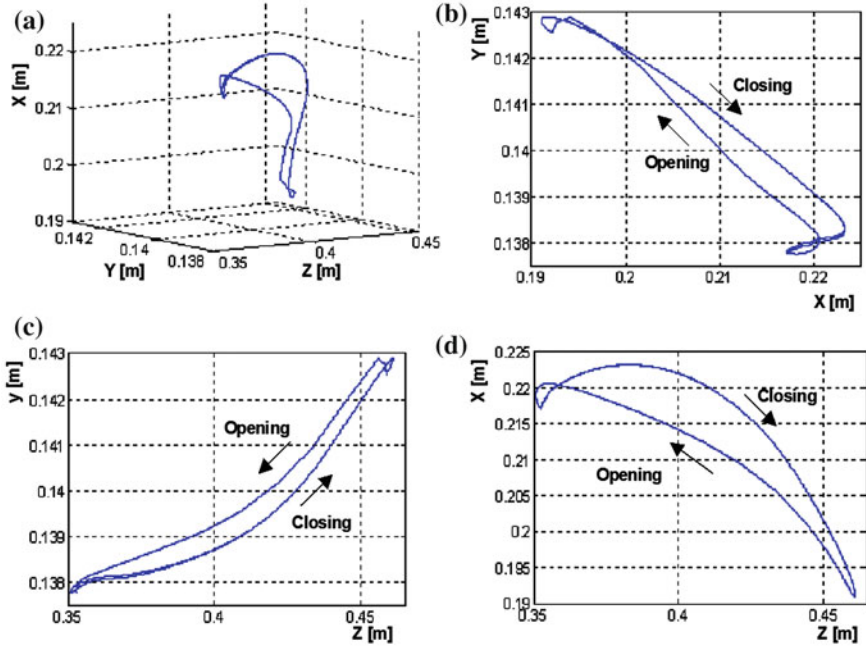


Fig. 2.28 Workspace of a fingertip motion of LARM Hand during an open-close operation mode: **a** A 3D view; **b** Projection onto XY plane; **c** Projection onto YZ plane; **d** Projection onto XZ plane

One should note that a nonzero value of the motion range in X direction is an evidence of a slightly nonplanar motion of the finger mechanism. This motion can be although as given by a certain clearance in the joints. Moreover, due to the presence of this clearance, the motion in the closing phase does not coincide with the motion in the opening phase as shown in Fig. 2.28. However, the above-mentioned motion ranges show a good match with those referring to a cylindrical grasping mode by an average human hand.

Additional experimental tests with the same set up have been carried in static conditions by applying known wrenches on the LARM Hand fingertip. Maximum compliant displacement that have been measured on the fingertip of LARM Hand has been of 0.1 mm for a maximum force of 3 N in the same direction. Thus, a stiffness coefficient can be computed as at least 30,000 N/m. The above-mentioned values of maximum compliant displacement and stiffness coefficient give a proof of a quite good stiffness behavior for LARM Hand operation, whose average grasping force is 3 N. A more accurate estimation of stiffness behavior can be obtained by computing a 6×6 Cartesian stiffness matrices for LARM Hand through a general procedure that has been proposed in [28].

2.7 Conclusions

This section has given fundamentals of stiffness modeling and analysis by referring to robotic systems for grasping tasks. A formulation has been detailed for the computation of the Cartesian stiffness matrix K . Considerations on local and global stiffness properties have been reported also within a numerical procedure. Cases of study have been proposed for the stiffness analysis of manipulators having serial or parallel architecture. Stiffness modeling and analysis has been reported also for mechanical end-effectors such as two-finger grippers or robotic hands, given their significance in grasping tasks. A procedure for experimental validation has been outlined and two cases of study have been reported.

References

1. Rivin EI (1999) Stiffness and damping in mechanical design. Marcel Dekker Inc., New York
2. Ceccarelli M (2004) Fundamentals of mechanics of robotic manipulation. Kluwer, Dordrecht
3. Tsai LW (1999) Robot analysis: the mechanics of serial and parallel manipulators. Wiley, New York, pp 260–297
4. Duffy J (1996) Statics and kinematics with applications to robotics. Cambridge University Press, Cambridge, pp 153–169
5. Nof SY (ed) (1985) Handbook of industrial robotics. Wiley, New York
6. Merlet J-P (2006) Parallel robots. Springer, Dordrecht
7. Carbone G (2003) Stiffness evaluation of multibody robotic systems. Ph D Dissertation, LARM, University of Cassino, Cassino
8. Gosselin C (1990) Stiffness mapping for parallel manipulators. IEEE Trans Robot Autom 6(3):377–382

9. Tahmasebi F, Tsai LW (1992) Jacobian and stiffness analysis of a novel class of six-dof parallel minimanipulators. In: Proceedings of the ASME 22nd biennial mechanism conference, Scottsdale, vol 47, pp 95–102
10. Gosselin CM, Zhang D (2002) Stiffness analysis of parallel mechanisms using a lumped model. *Int J Robot Autom* 17(1):17–27
11. Simaan N, Shoham M (2003) Stiffness synthesis of a variable geometry six-degrees-of-freedom double planar parallel robot. *Int J Robot Res* 22(9):757–775
12. Kim HY, Streit DA (1995) Configuration dependent stiffness of the Puma 560 manipulator: analytical and experimental results. *Mech Mach Theory* 30(8):1269–1277
13. Ceccarelli M, Carbone G (2005) Numerical and experimental analysis of the stiffness performance of parallel manipulators. In: 2nd international colloquium collaborative research centre 562, Braunschweig, pp 21–35
14. Chakarov D (2001) Analysis and synthesis of the stiffness of a hybrid manipulator with redundant actuation. In: Proceedings of the 5th Magdeburg days of mechanical engineering, Magdeburg, pp 119–127
15. Ciblak N, Lipkin H (1999) Synthesis of cartesian stiffness for robotic applications. In: Proceedings of the IEEE international conference on robotics and automation ICRA'99, Detroit, vol 3, pp 2147–2152
16. Pigoski T, Griffis M, Duffy J (1998) Stiffness mappings employing different frames of reference. *Mech Mach Theory* 33(6):825–838
17. Carbone G, Ceccarelli M (2004) A stiffness analysis for a hybrid parallel-serial manipulator. *Robot Int J* 22:567–576
18. Ceccarelli M, Carbone G (2002) A stiffness analysis for CaPaMan (Cassino parallel manipulator). *Mech Mach Theory* 37(5):427–439
19. Svinin MM, Hosoe S, Uchiyama M, Luo ZW (2002) On the stiffness and stiffness control of redundant manipulators. In: IEEE international conference on robotics & automation ICRA 2002, Washington, pp 2393–2399
20. Cutkosky MR, Kao I (1989) Computing and controlling the compliance of a robotic hand. *IEEE Trans Robot Autom* 5(2):151–165
21. Tsumugiwa T, Yokogawa R, Hara K (2002) Variable impedance control with virtual stiffness for human-robot cooperative peg-in-hole task. In: Proceedings of the IEEE/RSJ international conference on intelligent robots and systems IROS'02, Lausanne, pp 1075–1081
22. Chakarov D (1998) Optimization synthesis of parallel manipulators with desired stiffness. *J Theor Appl Mech* 28(4). Available. <http://www.imbm.bas.bg/IMBM/LMS/Chakarov/TPM98.pdf>
23. Liu X-J, Jin Z-L, Gao F (2000) Optimum design of 3-dof spherical parallel manipulators with respect to the conditioning and stiffness indices. *Mech Mach Theory* 35(9):1257–1267
24. Carbone G, Ottaviano E, Ceccarelli M (2007) An optimum design procedure for both serial and parallel manipulators. *IMEchE Part C J Mech Eng Sci* 221(7):829–843
25. Huang S, Schimmels JM (2000) The bounds and realization of spatial compliances achieved with simple springs connected in parallel. *IEEE Trans Robot Autom* 14(3):466–475
26. Zefran M, Kumar V (1997) Affine connections for the cartesian stiffness matrix. In: Proceedings of the IEEE international conference on robotics and automation ICRA'97, Albuquerque, vol 2, pp 1376–1381
27. Howard S, Zefran M, Kumar V (1998) On the 6×6 Cartesian stiffness matrix for three-dimensional motions. *Mech Mach Theory* 33(4):389–408
28. Chen S-F, Kao I (2000) Geometrical method for modeling of asymmetric 6×6 cartesian stiffness matrix. In: Proceedings of the IEEE/RSJ international conference on intelligent robots and systems IROS2000, Takamatsu, pp 1217–1222
29. Pham DT, Heginbotham WB (1986) Robot grippers. IFS Publications Ltd, Bedford
30. Rosheim ME (1996) Robot surrogate: work in progress. In: International conference on robotics and automation, Minnesota, pp 399–403
31. Cutkosky MR (1989) On grasp choice, grasp model, and the design of hands for manufacturing tasks. *IEEE Trans Robot Autom* 5(3):269–279

32. Iberal T (1997) Human prehension and dexterous robot hands. *Int J Robot Res* 6(3):285–299
33. Fukaya N, Toyama S, Asfour T, Dillmann R (2000) Design of the TUAT/Karlsruhe humanoid hand. In: *IEEE/RSJ international conference on intelligent robots and systems*, Takamatsu, vol 3, pp 1754–1759
34. Butterfass J, Grebenstein M, Liu H, Hirzinger G (2001) DLR-Hand II: next generation of a dexterous robot hand. In: *IEEE international conference on robotics and automation*, Seoul Korea, pp 109–114
35. Zhang Y, Han Z, Zhan H, Shang X, Wang T, Guo W (2001) Design and control of the BUAA four-fingered hand. *IEEE Trans Robot Autom* 3:2517–2522
36. Gosselin CM, Mountambault S, Gosselin CJ (1993) Manus Colobi: preliminary results on the design of a mechanical hand for industrial applications. In: *19th ASME design automation*, Albuquerque, vol 65–1, pp 585–592
37. Dechev N, Cleghorn WL, Nauman S (1999) Multiple finger, passive adaptive grasp prosthetic hand. *Mech Mach Theory* 36:1157–1173
38. Townsend WT (2000) The Barrethand grasper—programmably flexible parts handling and assembly. *Ind Robot Int J* 27(3):181–188
39. Venkataraman ST, Iberall T (eds) (1989) *Dexterous robot hands*. Springer, New York
40. Boudreault E, Gosselin C (2006) Design of sub-centimetre underactuated compliant gripper. In: *Proceedings of IDETC/CIE 2006 ASME 2006, 30th mechanisms & robotics conference*, Philadelphia. Paper DETC2006-99415
41. Ceccarelli M, Luyckx I, Vanaelten W (1996) Grasp forces in two-finger grippers: modeling and measuring. In: *5th international workshop on robotics in Alpe-Andria Danube region RAAD'96*, Budapest, pp 321–326
42. Ceccarelli M, Nava Rodriguez NE, Carbone G (2006) Design and tests of a three-finger hand with 1-dof articulated fingers. *Robot Int J* 24(2):183–196
43. Carbone G, González A (2011) Numerical simulation of the grasp operation by LARM hand IV, A three finger robotic hand. *Robot Comput Integr Manuf* 27(2):450–459
44. Carbone G, Jeckel M, Havlík S, Ceccarelli M (2003) An optimum multi-objective design procedure for microgripping mechanisms. In: *12th international workshop on robotics in Alpe-Andria-Danube region RAAD 2003*, Cassino, paper 055RAAD03
45. Penisi OH, Carbone G, Ceccarelli M (2002) Optimum design and testing of mechanisms for two-finger grippers. *Int J Mech Control* 03(01):9–20
46. Ceccarelli M, Carbone G, Kerle H (2001) Designing mechanisms for two-finger microgrippers. In: *CD proceedings of the 10th workshop on robotics and Alpe-Adria-Danube region RAAD'01*, Wien, paper RD-021
47. Carbone G, Ceccarelli M, Kerle H, Raatz A (2001) Design and experimental validation of a microgripper. *Fuji Int J Robot Mechatron* 13(3):319–325
48. Ceccarelli M, Carbone G (2010) Design and operation of fingered hands and two-finger grippers for space applications as from experiences at LARM. In: *IX international scientific-technical conference. Control vibration technologies and machines VIBRATION 2010*, Kursk, pp 208–216 (in Russian) ISBN 978-5-7681-0561
49. Lanni C, Carbone G, Havlík Š, Ceccarelli M (2007) Experimental validation of a milligripper based on Chebyshev mechanism. In: *Proceedings of the 16th international workshop on robotics in Alpe-Adria-Danube region*, Ljubljana, CD Proceedings, paper n. FP_GG2, pp 42–51
50. Vaishnav RN, Magrab EB (1987) A general procedure to evaluate robot positioning errors. *Int J Robot Res* 6(1):59–74
51. ANSI, American National Standards Institute (1990) American national standard for industrial robots and robot systems: point-to-point and static performance characteristics—evaluation. ANSI/RIA 15.05-1-1990, New York
52. UNI, Italian National Institute for Standards (1995) Manipulating industrial robots: performance criteria and related test methods. UNI EN 29283 (= ISO 9283), Milan

53. Carbone G, Ceccarelli M (2004) A procedure for experimental evaluation of Cartesian stiffness matrix. In: 15th CISM-IFTOMM symposium on robot design, dynamics and control, paper Rom04-24, Montreal
54. Carbone G, Ceccarelli M (2010) A comparison of indices for stiffness performance evaluation. *Front Mech Eng* 5(3):270–278. doi:[10.1007/s11465-010-0023-z](https://doi.org/10.1007/s11465-010-0023-z)
55. Pratt GA, Williamson MM, Dillworth P, Pratt J, Ulland K, Wright A (1995) Stiffness isn't everything. In: Preprints of the 4th international symposium on experimental robotics ISER'95, Stanford, available. http://www.ai.mit.edu/projects/leglab/publications/stiffness_isnt_everything.pdf
56. Schimmels JM (2001) Multidirectional compliance and constraint for improved robotic deburring. Part 1: improved positioning. *Robot Comput Integr Manuf* 17(4):277–286
57. English CE, Russell D (1999) Mechanics and stiffness limitations of a variable stiffness actuator for use in prosthetic limbs. *Mech Mach Theory* 34(1):7–25
58. Alici G, Shirinzadeh B (2003) Exact stiffness analysis and mapping for a 3-SPS + S parallel manipulator. In: 7th international conference on automation technology AUTOMATION 2003, Taiwan, paper F120
59. Zhou Y, Nelson BJ (1998) Adhesion force modeling and measurement for micromanipulation, microrobotics and micromanipulation. In: Sulzmann A, Nelson BJ (eds) *International society for optical engineering*, vol 3519. SPIE, Boston, pp 169–180
60. MSC.ADAMS (2010) Documentation and Help. User CD-ROM



<http://www.springer.com/978-1-4471-4663-6>

Grasping in Robotics

Carbone, G. (Ed.)

2013, VIII, 468 p., Hardcover

ISBN: 978-1-4471-4663-6